Quaternary Science Reviews 335 (2024) 108737

Contents lists available at ScienceDirect

Quaternary Science Reviews

journal homepage: www.elsevier.com/locate/quascirev

Tracking rapid ice recession in a major Southern Alps valley during the last glacial termination

Peter D. Strand [a,*], Aaron E. Putnam [a], Joerg M. Schaefer [b], George H. Denton [a], David J.A. Barrell [c]

[a] Department of Earth Sciences & Climate Change Institute, University of Maine, Orono, ME, 04469, USA
[b] Lamont-Doherty Earth Observatory, 61 Rt. 9W, Palisades, NY, 10964, USA
[c] GNS Science, Private Bag 1930, Dunedin, 9054, New Zealand

ARTICLE INFO

Handling Editor: Dr C. O'Cofaigh

Keywords:
New Zealand
Pleistocene
Cosmogenic isotopes
Glacial geomorphology
Southern Alps
Last glacial termination

ABSTRACT

The last glacial termination featured a major reconfiguration of Earth's climate and cryosphere, whose underlying cause remains unresolved. To investigate this problem, we combine ^{10}Be surface-exposure dating of moraines with former equilibrium line altitudes to determine the magnitude and timing of atmospheric temperature warming that ended the Last Glaciation in the Takapō/Tekapo valley in the central Southern Alps of New Zealand. We show mountain-valley glacier recession from a nearly full-glacial configuration to a near-interglacial configuration early in the termination between ~18,000 and ~17,000 yrs ago, commensurate with a net atmospheric warming of ~3.8 °C (from −6.25 °C to −2.5 °C cooler than present). Similar recession also affected mid-latitude mountain glaciers in South America. We suggest trans-South Pacific glacier withdrawal early in the termination resulted from a decisive poleward shift of the austral westerlies that increased the proportion of warm subtropical air masses flowing over southern mid-latitude mountains, markedly raising glacier ablation rates. Farther south, the poleward-shifted westerlies drove increased ocean upwelling and surface warming, outgassing of carbon dioxide, and progressive ocean destratification, together raising atmospheric temperature over the Antarctic Ice Sheet, but at a rate slower than over mid-latitude mountain glaciers. Overall, we consider that Southern Hemisphere middle-latitude glacier recession was linked to Antarctic warming by a poleward displacement in latitude and an increase in strength of the Southern Hemisphere westerlies.

1. Introduction

Glaciers in the Southern Alps of New Zealand lie between the belts of subtropical highs and subpolar lows that demarcate the austral westerly winds over the southwestern Pacific Ocean (Harrington, 1952; Bostock et al., 2013, 2015; Lorrey et al., 2022; Audet et al., 2022) (Fig. 1). These glaciers are sensitive monitors of atmosphere temperature because of rapid ice throughflow from accumulation to melting zones in a high-precipitation maritime environment (Anderson et al., 2010; Anderson and Mackintosh, 2006; Oerlemans, 1997; Mackintosh et al., 2017). Therefore, Southern Alps glaciers are well suited to monitor atmospheric temperature changes and associated latitudinal shifts of the austral westerly wind belt.

Traditional Earth system hypotheses calling on low-frequency forcing to govern global climate on ice age timescales have not provided an adequate explanation for the rapidity of transitions between glacial and interglacial climate states (Broecker and van Donk, 1970; Broecker and Denton, 1990). The underlying cause of transitional "jumps" (Broecker and Denton, 1989) that punctuate stable modes of climate operation remains unsettled. One prominent hypothesis posits that the last glacial termination was driven by increased radiative forcing across the globe because of rising atmospheric CO_2 levels (Shakun et al., 2012; Broecker, 2014), while a related hypothesis attributes the combined effects of decreasing ice-sheet albedo from shrinking Northern Hemisphere ice sheets and rising atmospheric CO_2 as causing the last glacial termination (Marcott et al., 2019; Tierney et al., 2020; Osman et al., 2021). Another notable hypothesis suggests that a 'bipolar seesaw' in heat distribution operated through the ocean during the last glacial termination, warming the Southern Hemisphere at the expense of the Northern Hemisphere and vice-versa (Crowley, 1992; Broecker, 1998; Barker et al., 2009). Still others have suggested that interhemispheric connections during the last glacial termination occurred primarily through the atmosphere via

---

* Corresponding author.
E-mail address: peter.strand@maine.edu (P.D. Strand).

https://doi.org/10.1016/j.quascirev.2024.108737
Received 8 February 2024; Received in revised form 14 May 2024; Accepted 22 May 2024

shifting wind patterns (Denton et al., 2010, 2021). Here we aim to discriminate among leading climate hypotheses by investigating the relative speed and magnitude of atmospheric warming over New Zealand as recorded by mountain glaciers. If Southern Hemisphere mid-latitude deglacial atmospheric warming followed the pattern of decreasing ice-sheet albedo and rising atmospheric CO_2, then traditional low-frequency Earth system hypotheses may be sufficient for explaining the last glacial termination of the Southern Hemisphere mid-latitudes. However, if the deglacial atmospheric warming led changes registered in the Southern Ocean and over the Antarctic continent at the end of the Last Glaciation, then alternative climate explanations are required.

In this paper we document the glacial history of the Takapō/Tekapo catchment (44°S, 170°E) as a case example of Southern Alps deglaciation. This catchment contains well-preserved glacial landforms, including moraine ridges, drumlins, glaciofluvial outwash plains and ice-molded bedrock, that afford physical evidence for former glacier-extents (Barrell et al., 2011; Sutherland et al., 2019a, 2019b, 2022). During the Last Glaciation the Takapō/Tekapo catchment featured three long ice tongues (Cass, Godley, Macaulay) that together coalesced into a large glacier that extended southward from the mountain front, and is referred to here as the Takapō/Tekapo glacier. Mapping of moraines formed by the main glacier during maximum glaciation and in its Cass tributary during deglaciation, together with ^{10}Be surface-exposure dating, allowed us to obtain a chronology of glacier margin changes, linked to snowline elevation changes during the glacial-to-interglacial transition in this catchment system.

2. Setting

During recent glaciations, glacier tongues extended from extensive icefields in the Southern Alps to feed local piedmonts. Post-glacial lakes such as Ohau, Pukaki, and Takapō/Tekapo occupy the lower reaches of the troughs of their former valley glaciers at the margin of the Mackenzie Basin (Fig. 2). Extensive lateral and terminal moraine sequences are preserved along the flanks of many of the glacier troughs. Mesozoic-age bedrock of the eastern side of the Southern Alps mostly comprises quartzo-feldspathic greywacke sandstone and argillite mudstone (Cox and Barrell, 2007), with glacially-transported greywacke boulders providing targets for surface exposure age dating. The landforms of the Southern Alps of New Zealand afford a record of glacier activity during and since the Last Glaciation (Suggate and Almond, 2005; Schaefer et al., 2006, 2015; Barrell et al., 2011; Kelley et al., 2014; Doughty et al., 2015; Strand et al., 2019). Variations of glaciers in the Southern Alps are controlled by the summer melt season and the glaciers adjust quickly to atmospheric temperature changes (Oerlemans, 1994; Anderson and Mackintosh, 2006; Anderson et al., 2010; Doughty et al., 2013; Mackintosh et al., 2017). As a result these glaciers afford quantitative insight into past climate conditions. Detailed studies have been completed previously on the Pleistocene to Holocene moraine sequences of three large valley catchments draining the eastern side of the Southern Alps, the Pukaki valley (Schaefer et al., 2006, 2009, 2015; Putnam et al., 2010; Kaplan et al., 2013; Kelley et al., 2014; Doughty et al., 2015; Strand et al., 2019; Denton et al., 2021), the Ohau valley (Kaplan et al., 2010; Putnam et al., 2013a), and the Rakaia valley, located about 120 km to the northeast of the Takapō/Tekapo valley (Putnam et al., 2013b; Rother et al., 2014; Koffman et al., 2017). Studies of a more reconnaissance nature have provided chronologies for parts of the moraine sequences of the Ahuriri valley, immediately southwest of the Ohau catchment (Tielidze et al., 2022, 2023), the Rangitata valley lying between the Takapō/Tekapo and Rakaia valleys (Barrell et al., 2019, and references therein), and the Waimakariri valley, immediately northeast of the Rakaia valley (Rother et al., 2015).

The Takapō/Tekapo valley has a north-south orientation. Lake Takapō/Tekapo lies in the deeper part of the former glacier trough, with well-preserved lateral or terminal moraines outboard of its southern, eastern, and western shores marking the limit of the ice-age glacier (Fig. 2). Of the catchment's three main tributaries, the Cass, Godley, and Macaulay valleys, we focused our investigation on the Cass valley, and two of its headwater tributary valleys, where particularly well-preserved lateral moraines provided suitable targets for ^{10}Be surface-exposure dating and former equilibrium-line altitude (ELA) estimations. These two small tributaries occupy hanging valleys that drain from the

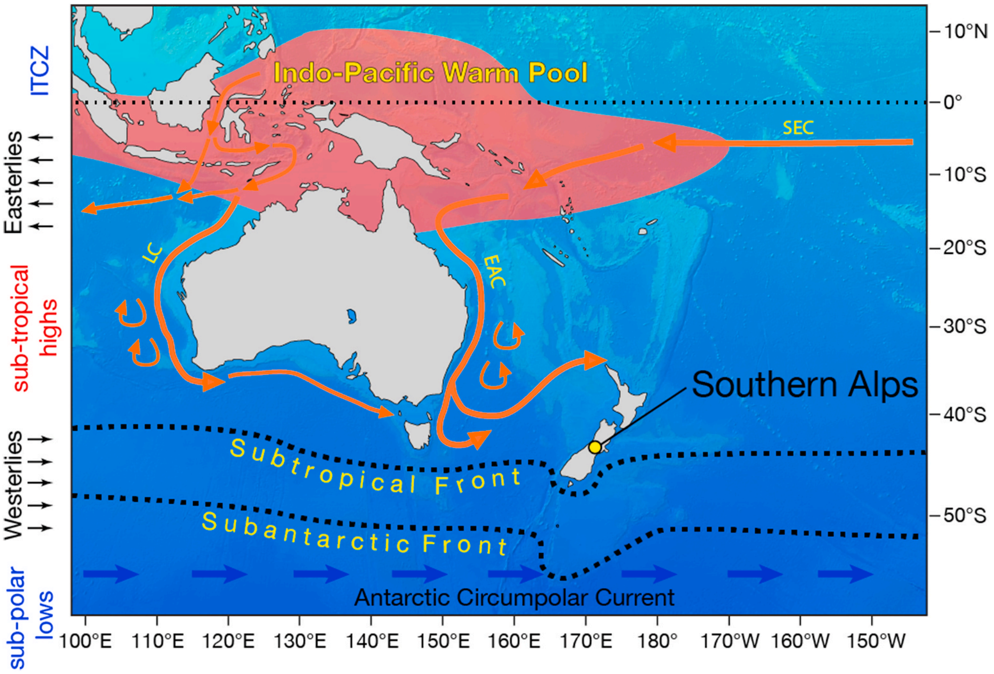

Fig. 1. Modern oceanic and atmospheric circulation of the Australasian sector of the Southern Hemisphere. New Zealand is located just north of the Subtropical Front and within the path of the Southern Hemisphere westerly wind belt. Arrows depict generalized ocean currents. LC: Leeuwin Current; EAC: East Australian Current; SEC: South Equatorial Current. Figure based on information from Carter et al. (1998); De Deckker et al. (2012); Putnam et al. (2012); Strand et al. (2019) and Moros et al. (2021).

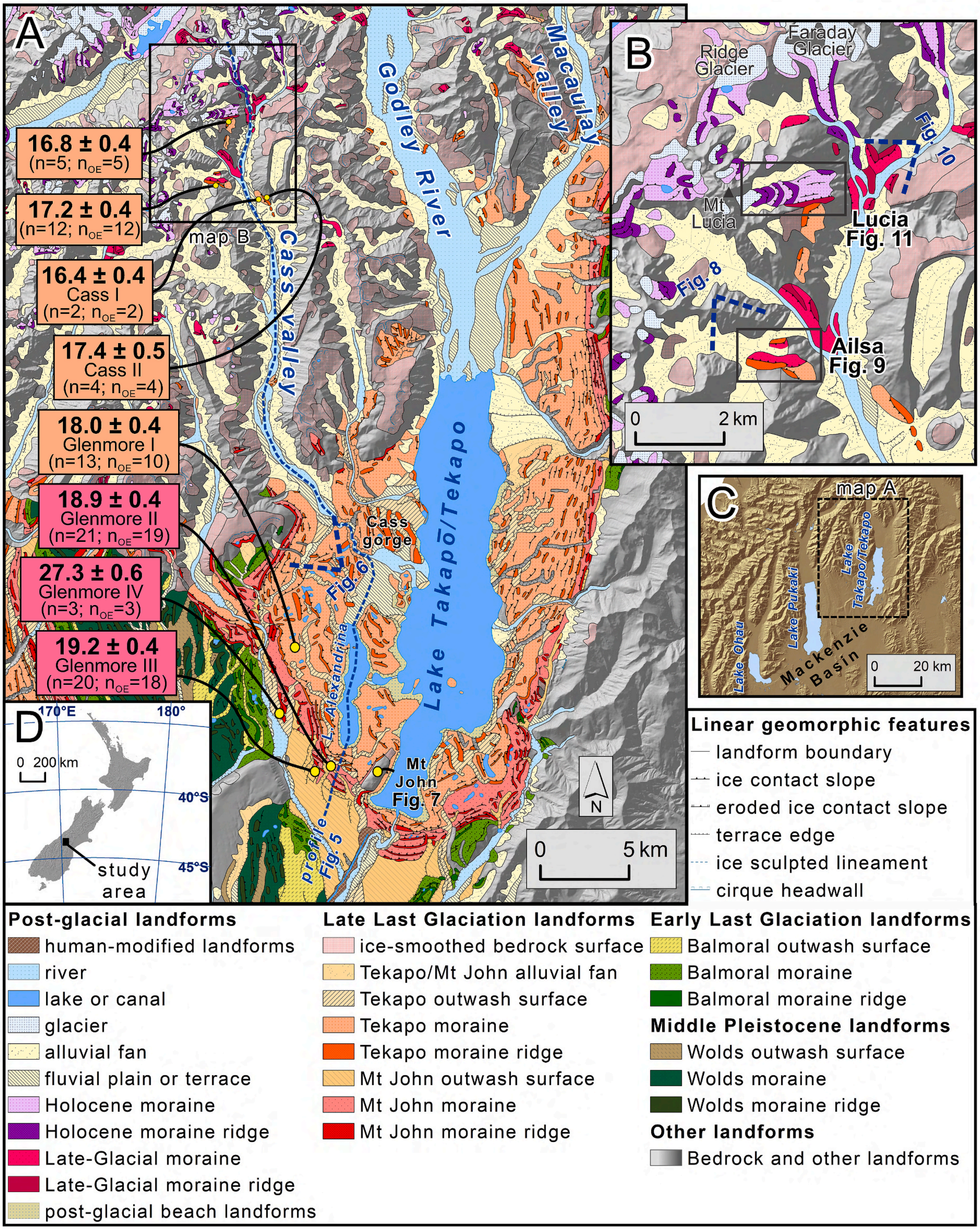

Fig. 2. Location and setting of the study area. A and B: glacial geomorphology map and legend after Barrell et al. (2011, 2013), with minor amendments. Yellow dots are general locations of targeted dating areas. Mean landform ages (kyrs) for the Last Glacial (Glenmore) and deglacial (Cass) moraines (Table 4) are discussed in the Results section, while Figs. 8–11 give ages for late-glacial and Holocene moraines. n = number of samples dated, N_{OE} = number of samples dated, with outlier ages excluded. Blue dotted line is Cass valley profile location (Fig. 5). Dark blue dashed lines indicate approximate fields of view in Figs. 6, 8 and 10. C and D are location maps.

Gamack Range at the western margin of the Cass valley. These tributaries do not have formal geographic names. One is a southern fork of the valley of Ailsa Stream and is referred to in shorthand here as the Ailsa valley. The other is a hanging-valley basin on the east side of Mt Lucia, the highest peak in the Gamack Range (2617 m a.s.l.) and is referred to here as the Lucia valley (Fig. 2). Glacial morphostratigraphic names follow those used in the Pukaki catchment by Barrell (2014), Barrell and Read (2014) and Denton et al. (2021).

3. Methods

3.1. Glacial geomorphologic mapping

Glacial geomorphologic maps provide a foundation for the interpretation of glacial history and give context for surface-exposure dating (Fig. 2). For the most part, the study used the approach and regional-scale maps of Barrell et al. (2011, 2013), with more detailed maps made in the Ailsa and Lucia areas of the Cass valley, and minor adjustments made to the regional-scale map to accommodate the findings from mapping and dating of this study. For the detailed mapping, glacial geomorphologic landforms were differentiated using a combination of field observations, topographic information and satellite imagery. Generalized topographic information came from an 8 m resolution digital elevation model (DEM) from Toitū Te Whenua Land Information New Zealand (LINZ). More detailed topographic information was acquired in the field using a DJI Phantom 4 drone and the Map Pilot software for Apple iPad. High-resolution orthoimage mosaics and DEMs (resolution ~50 cm/px) were produced photogrammetrically from the drone-acquired images using the Agisoft MetaShapePro software package, and georeferenced using ground-control points established with differential GPS techniques.

3.2. Field and laboratory procedures for ^{10}Be surface-exposure dating

Our field protocols for ^{10}Be surface-exposure sampling follow the approach of Putnam et al. (2010) and Strand et al. (2019). We collected rock samples from large boulders embedded in stable positions on well-preserved moraine ridges and glacial erratic boulders resting upon ice-molded bedrock surfaces. Boulders in the study area are predominantly quartzo-feldspathic greywacke sandstone, and we targeted boulders that had even, flat-topped surfaces. Boulders showing evidence for disturbance by fluvial processes, slope movement, or human activities were avoided. We sampled several boulders from each glacial landform feature (e.g. moraine ridge or ice-molded bedrock surface). Examples of sampled boulders are shown in Fig. 3. Samples were collected using the methods of Kelly et al. (2008) with locations measured using a Trimble Geo7x GPS instrument. Location measurements were later corrected differentially against data from the Mount John Observatory base station (UNAVCO site code 'MTJO'). Horizontal and vertical uncertainties for differentially corrected GPS measurements were typically less than ±1 m. A compass-clinometer or Theodolite™

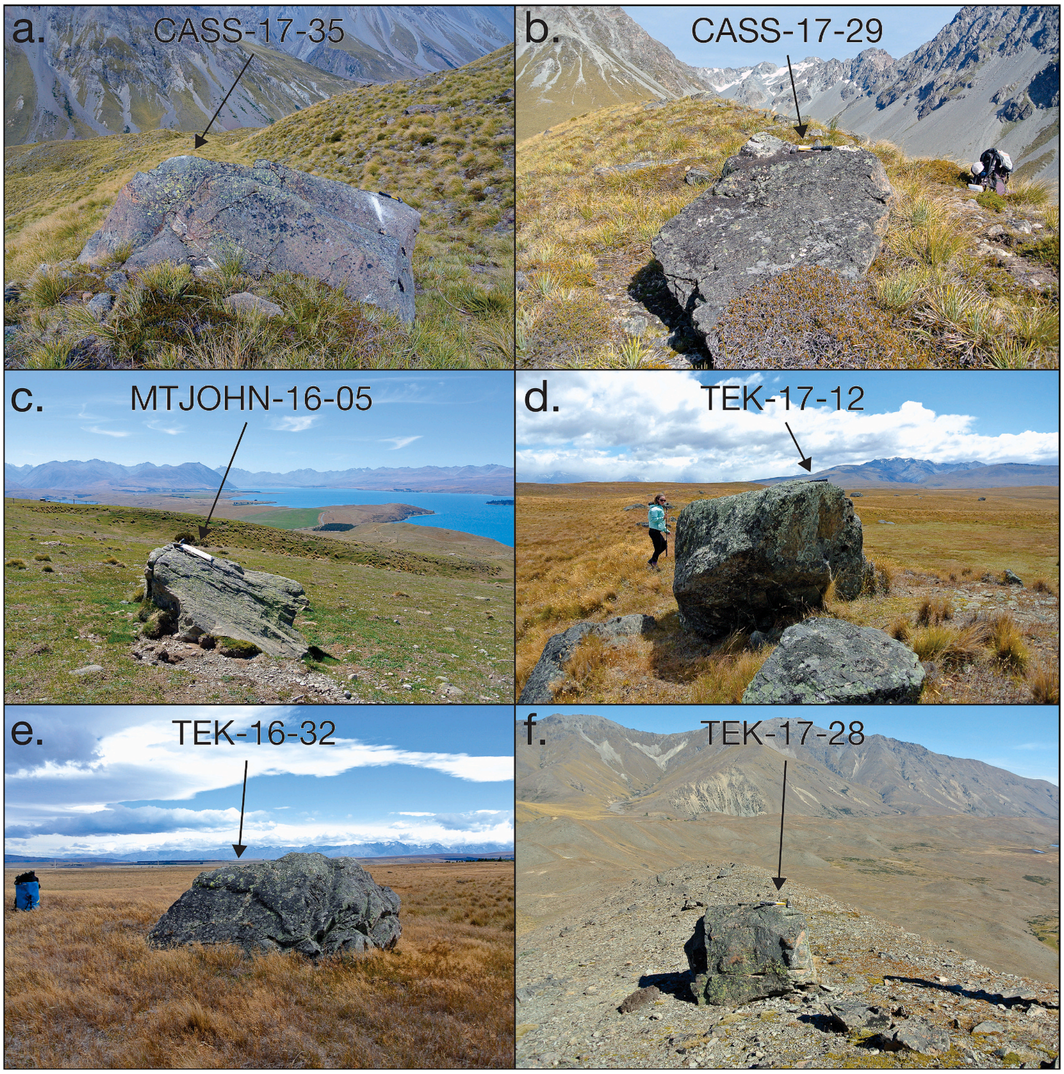

Fig. 3. Illustrations of representative boulders sampled for ^{10}Be surface-exposure dating, annotated with sample ID. **a.** Looking east-southeast to a ~1 m high boulder on the Ailsa I moraine. **b.** Westward view of a ~1 m high boulder on the Ailsa II moraine. **c.** Glacial erratic boulder resting on the till-mantled bedrock of Mt John, with Lake Takapō/Tekapo away to the north-northeast. **d.** Large boulder rooted in a Glenmore I moraine ridge, looking west-northwest. **e.** Southeastward view of a large boulder embedded in the Glenmore II moraine. **f.** ~1 m high boulder on the Glenmore III moraine, looking southeast.

application on an Apple iPad was used to chart the azimuth and bearing, respectively, of the surrounding skyline for determining topographic shielding corrections. We measured the dip angle and dip direction of each surface targeted for sampling using either a Brunton compass or else the GeoID™ application on an Apple iPad. Topographic shielding corrections were calculated using the University of Washington (UW) online calculator available at: https://hess.ess.washington.edu/. Each boulder was photographed and sketched from several vantages.

A total of 135 samples were processed at the Lamont-Doherty Earth Observatory Cosmogenic Isotope Laboratory following the methods of Schaefer et al. (2009), and references therein (Table 1). The Cosmogenic Isotope Laboratory procedures include both the physical and the chemical preparation of samples, as described online at http://www.ldeo.columbia.edu/res/pi/tcn/. Whole-rock samples were crushed to 125–710 μm grain-size fractions and boiled in H_3PO_4 and NaOH solutions. Samples were then subjected to several rounds of etching in 2% and 5% HF/HNO_3 solutions to isolate quartz. The quartz extracts were weighed, spiked with ~0.2 g of ^{9}Be-carrier, and dissolved in concentrated HF. The ^{9}Be carriers LDEO-4, LDEO-5 or LDEO-6 were used for this study (Table 2). All beryllium carrier concentrations were corrected for evaporation effects following Putnam et al. (2019). Samples were subjected to chromatography techniques to isolate the beryllium fraction. The CAMS accelerator at the Lawrence-Livermore National Laboratory was employed to measure the ratio of ^{10}Be to ^{9}Be. Samples were measured relative to the 07KNSTD standard ($^{10}Be/^9Be = 2.85e^{-12}$) (Nishiizumi et al., 2007). Measurements were corrected for boron contamination and for ^{10}Be in procedural blanks. Reported sample ^{10}Be concentration uncertainties have been propagated with uncertainties attending measured blank ^{10}Be concentrations (Table 1). Analytical uncertainties are generally ~2%.

3.3. Age calculations

We calculated surface-exposure ages using the Putnam et al. (2010) ^{10}Be production rate calibration data set from the Macaulay valley (Fig. 2), together with the time-independent scaling method of Lal (1991) and Stone (2000) ('St') and a time-dependent scaling version of Lal (1991) and Stone (2000) that incorporates the high-resolution geomagnetic model of Lifton et al. (2008) ('Lm'). Calculations were carried out using a wrapper MATLAB script, modified from the CRONUS-Earth online calculator, version 2 (Balco et al., 2008), following Strand et al. (2019) and Denton et al. (2021). Individual exposure ages are reported with 1σ analytical uncertainties, grouped according to the glacial landform feature that was sampled. All ages are reported to one digit beyond the significant figure, following the convention set forth by Stuiver and Polach (1977). Exposure ages are regarded as outliers if they are out of morphostratigraphic order or differ from other ages on the same glacial landform feature in a statistically significant way (as determined using Peirce's criterion or χ^2 statistics). Outliers are excluded from statistical analyses. Collective 'landform' ages are calculated from the individual ages of each glacial landform set, reported as arithmetic mean along with both the standard error of the mean and an 'external uncertainty' that includes the standard error propagated in quadrature with the production-rate uncertainty.

In this paper we follow similar Southern Alps studies (Putnam et al., 2013a, 2013b; Kelley et al., 2014; Doughty et al., 2015; Schaefer et al., 2015; Strand et al., 2019; Denton et al., 2021) and discuss ages calculated using the Putnam et al. (2010) calibration data set and the "Lm" scaling protocol of (Lal, 1991; Stone, 2000; Lifton et al., 2008). The "Lm" scaling protocol affords the best agreement with nearby independent radiocarbon age controls (Putnam et al., 2010). We note that the 'LSDn' scaling protocol (Lifton et al., 2014, 2016), as employed in the UW exposure-age calculator, gives ages that are inconsistent with radiocarbon age control, and we caution against its use elsewhere in settings where exposure ages cannot be verified by independent age control (see Appendix A).

3.4. Glacier ELA estimation methods

The equilibrium-line altitudes (ELAs) of mountain glaciers are related to climatic conditions and the estimation of former ELAs generates a valuable proxy for paleoclimatic information in mountain regions (Benn and Lehmkuhl, 2000). We used the maximum elevation of lateral moraine (MELM) method to estimate former glacier ELAs in the Takapō/Tekapo catchment. In New Zealand, the annual end-of-summer snowline measured on modern glaciers is taken as an approximation of the ELA (Chinn, 1999). Because glacier ablation, and hence ice-marginal deposition of glaciogenic sediment, only occurs at elevations lower than the ELA, the ELA must lie above the highest lateral moraines (Lichtenecker, 1938; Andrews, 1975; Meierding, 1982). Benn and Lehmkuhl (2000) advocate the MELM method as the most reliable method of ELA estimation where lateral moraines of a former glacier are well preserved, as it does not require complete reconstruction of the former glacier surface; the elevation of a well-preserved upper limit of a lateral moraine defines a minimum elevation for the ELA of the glacier that formed the moraine.

Our application of the MELM method in the Takapō/Tekapo catchment allowed us to estimate ELAs of paleo-glaciers directly from the elevation of mapped and dated lateral moraine sequences in the Cass valley. Our Last Glacial data point comes from the lower Cass valley (Fig. 6), and the deglacial, late glacial and Holocene data are from the Lucia valley (Fig. 2; also Figs. 8 and 11). A marked change in glacier geometry occurred in the Lucia valley at the start of the Holocene. The deglacial and late-glacial moraines relate to a valley-filling glacier fed from much of the valley headwall, but the earliest Holocene and younger moraines were associated with a more localized glacier fed mainly from the highest part of the catchment. Thus, the smaller glacier was fed by a relatively higher-altitude catchment headwall than was the case for the late glacial valley-filling glacier. As a result, the Holocene snowline was relatively low compared to the late glacial snowline. Contemporary snowline trends from Chinn (1995) indicate that the 'steady-state' ELA surface (at approximately AD 1976) is slightly higher than 2200 m a.s.l. at this location. This is constrained observationally at the Ridge Glacier, 3 km to the NW (Fig. 2), with an assigned 'steady-state' ELA of 2260 m a.s.l. (Chinn, 1995). The farthest upstream moraine of the Lucia valley (likely pre-industrial age) has a MELM of 2040 m a.s.l. Rounded to the nearest 50 m, we suggest that the Holocene MELM values for the Lucia valley are ~150 m anomalously low compared to regional trends. Accordingly, we added 150 m to the MELM-based ELA to obtain "adjusted ELA" for the Holocene moraines. We present both the adjusted and non-adjusted ELA (Fig. 6) and note that preferring one or the other does not change our conclusions. We converted the MELM-based estimates of paleo-ELAs into paleo-temperatures using the local lapse rate of 5 °C km^{-1}, which has been shown to be appropriate for alpine regions of New Zealand (Norton, 1985; Anderson et al., 2010; Golledge et al., 2012; Doughty et al., 2013; Eaves et al., 2017).

A need for interpretive caution arises from the question of incomplete lateral moraine preservation in steep mountain environments that may make the MELM value an ill-constrained minimum for the former ELA. However, the excellent preservation of the Lucia moraine sequence reflects a general absence of erosional modification of that valley, and thus we think any erosional excision of the upper limits of its moraine ridges has been minimal. Adjacent to the Lucia valley, the upper end of the deglacial moraine ridge peters out onto relict ice-smoothed bedrock terrain, giving us high confidence that its upper elevational limit reflects depositional processes.

4. Results

The geomorphological mapping illustrates the presence of a comprehensive sequence of moraines and other glaciogenic landforms in the Takapō/Tekapo catchment, spanning from the Last Glacial when ice extended out to the intermontane Mackenzie Basin, through to moraines

Table 1
^{10}Be sample details and analytical data.

Landform Name	Sample ID	CAMS Laboratory number	Latitude (DD)	Longitude (DD)	Elevation (m.a.s.l.)	Sample Thickness (cm)	Density (g cm-2)	Shielding correction	Quartz weight (g)	Carrier added (g)	Carrier conc. (ppm)	10Be/9Be ± 1σ (10–14)	[10Be] ± 1σ (104) (atoms/gram)
Lucia I	LUC-09-16	BE28272	−43.6478017	170.3653795	1983.54	2.66	2.7	0.961106	96.4548	0.1597	996.0	3.35 ± 0.13	0.36 ± 0.01
Lucia I	LUC-09-13	BE28271	−43.6485968	170.3639088	2026.87	3.27	2.7	0.937190	76.7660	0.1595	996.0	5.71 ± 0.13	0.77 ± 0.02
Lucia I	LUC-09-15	BE29487	−43.6481525	170.3647621	2005.78	2.58	2.7	0.955982	86.4995	0.1504	1025.9	44.97 ± 0.69	5.31 ± 0.08
Lucia II	LUC-09-20	BE29482	−43.6475303	170.3686886	1873.07	1.61	2.7	0.947950	20.6502	0.1510	1025.9	3.94 ± 0.22	1.91 ± 0.11
Lucia II	LUC-09-22	BE29483	−43.6473567	170.3688857	1868.35	1.93	2.7	0.950259	26.1010	0.1502	1025.9	5.17 ± 0.25	1.99 ± 0.1
Lucia II	LUC-09-21	BE40251	−43.6474358	170.3686956	1871.25	2.45	2.7	0.948713	30.0955	0.1829	1043.2	4.92 ± 0.15	2.06 ± 0.06
Lucia III	LUC-09-23	BE28274	−43.6457984	170.3689435	1873.36	1.80	2.7	0.955054	18.7189	0.1809	996.0	22.38 ± 0.36	14.3 ± 0.23
Lucia III	LUC-09-24	BE28275	−43.6458778	170.3690049	1871.73	1.38	2.7	0.955054	24.9257	0.1811	996.0	28.77 ± 1.13	13.84 ± 0.54
Lucia IV	LUC-09-26	BE28276	−43.6456353	170.3690564	1871.20	1.42	2.7	0.958141	25.0676	0.1786	996.0	30.02 ± 0.53	14.16 ± 0.25
Lucia IV	LUC-09-27	BE28277	−43.6456794	170.3691089	1869.78	2.05	2.7	0.958141	26.1244	0.1821	996.0	32.14 ± 0.52	14.84 ± 0.24
Lucia V	LUC-09-17	BE28870	−43.6474561	170.3698655	1847.61	1.22	2.7	0.955111	9.7596	0.1822	1024.9	12.39 ± 0.17	15.53 ± 0.21
Lucia V	LUC-09-18	BE28871	−43.6474663	170.3696868	1850.63	2.66	2.7	0.956055	9.2678	0.1830	1024.9	13.04 ± 0.16	17.31 ± 0.22
Lucia VI	LUC-09-30	BE28278	−43.6454507	170.3689989	1872.90	2.66	2.7	0.951292	26.1341	0.1811	996.0	35.46 ± 0.58	16.29 ± 0.27
Lucia VI	LUC-09-31	BE28872	−43.6480063	170.3685137	1872.84	0.97	2.7	0.941339	9.2725	0.1817	1024.9	12.13 ± 0.24	15.96 ± 0.32
Lucia VII	LUC-09-35	BE28873	−43.6459673	170.3729063	1811.70	1.39	2.7	0.970608	9.8947	0.1834	1024.9	14.94 ± 0.21	18.66 ± 0.26
Lucia VIII	LUC-09-37	BE29517	−43.6450620	170.3742068	1783.58	1.47	2.7	0.965435	10.6174	0.1818	1025.8	15.69 ± 0.22	18.21 ± 0.25
Lucia VIII	LUC-09-38	BE28874	−43.6454492	170.3747356	1777.52	1.91	2.7	0.972592	10.1601	0.1831	1024.9	15.01 ± 0.21	18.23 ± 0.26
Lucia VIII	LUC-09-41	BE28875	−43.6472069	170.3740974	1780.39	1.82	2.7	0.968962	10.4896	0.1830	1024.9	14.8 ± 0.26	17.4 ± 0.31
Lucia IX	LUC-09-42	BE28926	−43.6453772	170.3764542	1739.84	1.37	2.7	0.978046	9.5622	0.1821	996.0	13.78 ± 0.35	17.32 ± 0.44
Lucia IX	LUC-09-44	BE28924	−43.6458499	170.3772563	1725.86	1.52	2.7	0.978046	9.8292	0.1834	996.0	14.19 ± 0.22	17.48 ± 0.27
Lucia X	LUC-09-48	BE29516	−43.6467024	170.3792284	1694.94	3.43	2.7	0.980942	9.9995	0.1836	1025.8	14.62 ± 0.24	18.19 ± 0.3
Lucia XI	LUC-09-49	BE28876	−43.6463958	170.3798429	1691.58	2.10	2.7	0.982425	9.5413	0.1830	1024.9	12.78 ± 0.22	16.48 ± 0.29
Lucia XII	LUC-09-47	BE28852	−43.6476029	170.3783293	1707.90	1.38	2.7	0.977047	11.5276	0.1821	1024.3	16.11 ± 0.43	17.3 ± 0.47
Lucia XII	LUC-09-10	BE28869	−43.6478850	170.3735572	1787.88	1.44	2.7	0.963132	10.3089	0.1828	1024.9	16.24 ± 0.26	19.43 ± 0.31
Lucia XII	LUC-09-11	BE40249	−43.6479005	170.3735962	1786.22	2.89	2.7	0.963132	11.5371	0.1830	1043.2	16.24 ± 0.3	17.89 ± 0.34
Lucia XII	LUC-09-12	BE40250	−43.6478768	170.3741797	1774.64	1.50	2.7	0.943934	7.3088	0.1828	1043.2	10.94 ± 0.22	18.98 ± 0.39
Lucia XIII	LUC-09-06	BE40246	−43.6487218	170.3772691	1762.16	2.05	2.7	0.986319	15.0157	0.1833	1043.2	25.03 ± 0.58	21.25 ± 0.49
Lucia XIII	LUC-09-07	BE40247	−43.6487662	170.3771412	1762.10	2.03	2.7	0.986109	15.0082	0.1828	1043.2	25.36 ± 0.48	21.49 ± 0.4
Lucia XIII	LUC-09-08	BE28851	−43.6487666	170.3740143	1826.27	0.80	2.7	0.971735	10.8763	0.1829	1024.3	19.24 ± 0.29	22.01 ± 0.33
Lucia XIII	LUC-09-09	BE40248	−43.6487687	170.3739702	1826.48	1.67	2.7	0.971735	15.0278	0.1831	1043.2	25.59 ± 0.48	21.69 ± 0.4
Lucia XIV	LUC-09-01	BE28921	−43.6490272	170.3796158	1766.81	0.70	2.7	0.993667	8.1240	0.1833	996.0	18.08 ± 0.24	26.98 ± 0.35
Lucia XIV	LUC-09-02	BE28922	−43.6489972	170.3788505	1774.40	1.85	2.7	0.991426	7.9606	0.1816	996.0	17.81 ± 0.3	26.87 ± 0.46
Lucia XIV	LUC-09-03	BE28923	−43.6490742	170.3788510	1774.87	1.98	2.7	0.991426	8.5200	0.1819	996.0	19.81 ± 0.45	27.98 ± 0.63
Lucia XIV	LUC-09-04	BE28850	−43.6495846	170.3780070	1769.40	1.05	2.7	0.990393	10.7827	0.1820	1024.3	23.9 ± 0.28	27.49 ± 0.33
Lucia XIV	LUC-09-05	BE28925	−43.6489491	170.3779933	1765.14	0.86	2.7	0.988634	7.1514	0.1837	996.0	16.22 ± 0.25	27.54 ± 0.42
Ailsa I	CASS-17-33	BE44629	−43.6808229	170.3702298	1409.09	2.80	2.7	0.982585	8.4629	0.2015	1036.8	9.71 ± 0.22	15.91 ± 0.36
Ailsa I	CASS-17-35	BE44630	−43.6810932	170.3669377	1459.39	3.08	2.7	0.981746	7.0843	0.2023	1036.8	8.15 ± 0.15	16.01 ± 0.3
Ailsa I	CASS-17-36	BE44631	−43.6810689	170.3662045	1470.52	3.66	2.7	0.984452	7.7406	0.2011	1036.8	9.15 ± 0.17	16.36 ± 0.31
Ailsa II	CASS-17-26	BE42971	−43.6811395	170.3641307	1498.12	2.22	2.7	0.980948	6.5399	0.2025	1035.9	8.29 ± 0.17	17.72 ± 0.37
Ailsa II	CASS-17-27	BE44625	−43.6814198	170.3664066	1468.07	2.43	2.7	0.981288	8.8648	0.2023	1036.8	10.79 ± 0.23	16.97 ± 0.36
Ailsa II	CASS-17-28	BE44626	−43.6813371	170.3674990	1456.75	1.43	2.7	0.978207	7.1003	0.2017	1036.8	8.48 ± 0.18	16.58 ± 0.35
Ailsa II	CASS-17-29	BE44627	−43.6813624	170.3678685	1450.66	3.95	2.7	0.982396	8.4429	0.2024	1036.8	9.95 ± 0.19	16.42 ± 0.31
Ailsa II	CASS-17-30	BE42972	−43.6814361	170.3687497	1433.03	2.29	2.7	0.985260	7.5764	0.2024	1035.9	9.61 ± 0.22	17.73 ± 0.4
Ailsa II	CASS-17-31	BE44628	−43.6813960	170.3688665	1429.12	2.05	2.7	0.980807	8.4917	0.2026	1036.8	10.07 ± 0.2	16.55 ± 0.32
Ailsa II	CASS-17-32	BE42973	−43.6813883	170.3698570	1411.63	1.90	2.7	0.979178	6.6735	0.2028	1035.9	8.17 ± 0.16	17.14 ± 0.33
Ailsa III	CASS-17-22	BE42969	−43.6808764	170.3605347	1531.55	2.17	2.7	0.970081	6.5206	0.2023	1035.9	10.34 ± 0.19	22.15 ± 0.42
Ailsa III	CASS-17-23	BE42970	−43.6808598	170.3604981	1533.06	3.02	2.7	0.970177	6.3785	0.2027	1035.9	10.27 ± 0.21	22.55 ± 0.46
Ailsa IV	CASS-17-18	BE44621	−43.6825961	170.3730503	1370.25	1.17	2.7	0.976495	7.3778	0.2007	1036.8	10.94 ± 0.21	20.5 ± 0.39
Ailsa IV	CASS-17-19	BE44622	−43.6825191	170.3730254	1370.18	2.82	2.7	0.974230	7.2137	0.2013	1036.8	9.95 ± 0.19	19.12 ± 0.37
Ailsa IV	CASS-17-20	BE44623	−43.6824482	170.3728928	1372.06	2.11	2.7	0.978002	7.2291	0.2019	1036.8	10.11 ± 0.18	19.45 ± 0.34
Ailsa V	CASS-17-11	BE44620	−43.6832499	170.3749620	1344.30	1.31	2.7	0.980008	7.1070	0.1989	1036.8	10.22 ± 0.2	19.7 ± 0.38
Ailsa V	CASS-17-13	BE42964	−43.6826843	170.3723704	1386.88	1.83	2.7	0.977177	6.1943	0.2023	1035.9	9.03 ± 0.17	20.36 ± 0.38

(*continued on next page*)

Table 1 (*continued*)

Landform Name	Sample ID	CAMS Laboratory number	Latitude (DD)	Longitude (DD)	Elevation (m.a.s.l.)	Sample Thickness (cm)	Density (g cm-2)	Shielding correction	Quartz weight (g)	Carrier added (g)	Carrier conc. (ppm)	10Be/9Be ± 1σ (10–14)	[10Be] ± 1σ (104) (atoms/gram)
Ailsa V	CASS-17-14	BE42965	−43.6825544	170.3722489	1388.79	1.88	2.7	0.977186	5.2873	0.2027	1035.9	7.78 ± 0.15	20.59 ± 0.39
Ailsa V	CASS-17-15	BE42966	−43.6826842	170.3719904	1393.15	1.93	2.7	0.977176	6.3899	0.2026	1035.9	9.29 ± 0.17	20.34 ± 0.38
Ailsa V	CASS-17-16	BE42967	−43.6825982	170.3717083	1397.23	1.55	2.7	0.972729	2.7742	0.2029	1035.9	4.34 ± 0.12	21.84 ± 0.63
Ailsa VI	CASS-17-06	BE42962	−43.6830099	170.3650886	1512.81	2.27	2.7	0.974136	5.5238	0.2021	1035.9	9 ± 0.17	22.74 ± 0.43
Ailsa VI	CASS-17-09	BE42963	−43.6824417	170.3667899	1485.33	1.62	2.7	0.975869	5.5652	0.2017	1035.9	8.6 ± 0.21	21.52 ± 0.52
Cass I	CASS-14-05	BE40243	−43.6926624	170.4038720	1161.33	2.90	2.7	0.979341	15.0393	0.1824	1043.5	19.3 ± 0.36	16.28 ± 0.31
Cass I	CASS-14-06	BE40244	−43.6925637	170.4037244	1162.13	2.69	2.7	0.980049	15.0097	0.1826	1043.5	19.59 ± 0.5	16.57 ± 0.43
Cass II	CASS-14-01	BE40026	−43.6916464	170.4031071	1178.57	2.58	2.7	0.973795	15.0079	0.1837	1043.0	20.69 ± 0.39	17.62 ± 0.33
Cass II	CASS-14-02	BE40027	−43.6916707	170.4030874	1176.68	2.33	2.7	0.974864	15.0393	0.1834	1043.0	21.34 ± 0.68	18.11 ± 0.57
Cass II	CASS-14-03	BE40028	−43.6919551	170.4037230	1173.19	2.35	2.7	0.975762	15.0181	0.1830	1043.0	21.24 ± 0.39	18.01 ± 0.33
Cass II	CASS-14-04	BE40242	−43.6920862	170.4039081	1171.94	2.46	2.7	0.974236	15.0252	0.1823	1043.5	19.8 ± 0.37	16.7 ± 0.31
Glenmore I	TEK-16-12	BE41369	−43.9604699	170.4276147	843.43	2.87	2.7	0.997563	5.3638	0.1838	1028.1	6.07 ± 0.12	14.15 ± 0.28
Glenmore I	TEK-16-13	BE41370	−43.9506015	170.4253216	859.78	3.01	2.7	0.999961	7.2149	0.1836	1028.1	8.29 ± 0.16	14.39 ± 0.28
Glenmore I	TEK-16-16	BE41371	−43.9483657	170.4245926	861.54	4.36	2.7	0.999119	5.3378	0.1837	1028.1	6.15 ± 0.14	14.4 ± 0.32
Glenmore I	TEK-17-20	BE44617	−43.9768553	170.5546531	825.74	2.54	2.7	0.999148	5.0615	0.2025	1036.3	5.29 ± 0.16	14.5 ± 0.45
Glenmore I	TEK-17-21	BE44618	−43.9768258	170.5545950	824.80	1.94	2.7	0.999120	5.2290	0.2004	1036.3	5.11 ± 0.13	13.39 ± 0.34
Glenmore I	TEK-17-22	BE44619	−43.9767245	170.5545082	823.59	1.93	2.7	0.998887	5.0301	0.2014	1036.3	5.25 ± 0.13	14.39 ± 0.36
Glenmore I	TEK-18-04	BE44610	−43.9900986	170.5111788	766.13	1.57	2.7	0.994785	5.1251	0.2016	1036.3	4.93 ± 0.11	13.27 ± 0.31
Glenmore I	TEK-18-05	BE44611	−43.9901829	170.5110360	764.86	2.74	2.7	0.998064	5.1304	0.2020	1036.3	5 ± 0.13	13.48 ± 0.35
Glenmore I	TEK-17-11	BE44607	−43.9768246	170.4316625	824.24	0.87	2.7	0.999681	5.0169	0.2022	1036.2	5.53 ± 0.13	15.36 ± 0.36
Glenmore I	TEK-17-12	BE44608	−43.9770612	170.4322565	825.56	1.80	2.7	0.999542	2.6512	0.2016	1036.2	2.81 ± 0.08	14.65 ± 0.44
Glenmore I	TEK-17-13	BE42944	−43.9771862	170.4328656	825.94	1.69	2.7	0.999680	4.9862	0.1830	1034.4	5.54 ± 0.13	13.99 ± 0.34
Glenmore I	TEK-17-14	BE42945	−43.9771891	170.4330197	826.12	1.53	2.7	0.999979	2.1594	0.1830	1034.4	2.51 ± 0.09	14.55 ± 0.53
Glenmore I	TEK-17-15	BE42946	−43.9775637	170.4339227	823.31	2.22	2.7	0.999973	5.0571	0.1833	1034.4	6.05 ± 0.12	15.09 ± 0.3
Glenmore II	CASS-12-04	BE41374	−43.8476670	170.4124330	1298.00	2.03	2.7	0.996626	5.2179	0.1838	1028.1	8.97 ± 0.27	21.55 ± 0.65
Glenmore II	CASS-12-07	BE40018	−43.8556068	170.4185815	1141.14	2.26	2.7	0.996626	15.0148	0.1826	1043.0	22.1 ± 0.41	18.7 ± 0.35
Glenmore II	CASS-12-08	BE40019	−43.8555508	170.4185670	1141.78	0.80	2.7	0.996626	15.0112	0.1827	1043.0	23.17 ± 0.43	19.62 ± 0.37
Glenmore II	CASS-12-09	BE40020	−43.8554807	170.4186534	1140.43	1.49	2.7	0.996626	15.0344	0.1827	1043.0	22.52 ± 0.42	19.04 ± 0.36
Glenmore II	CASS-12-10	BE40021	−43.8552872	170.4186259	1141.26	2.12	2.7	0.995609	15.0090	0.1830	1043.0	23.12 ± 0.43	19.61 ± 0.37
Glenmore II	CASS-12-11	BE40022	−43.8552519	170.4185898	1140.91	1.56	2.7	0.995609	15.0840	0.1833	1043.0	22.79 ± 0.43	19.27 ± 0.36
Glenmore II	CASS-12-12	BE40023	−43.8543241	170.4195266	1141.43	2.83	2.7	0.994604	15.0047	0.1834	1043.0	22.47 ± 0.42	19.12 ± 0.36
Glenmore II	CASS-12-13	BE40024	−43.8553085	170.4195342	1127.81	1.04	2.7	0.979601	15.0270	0.1835	1043.0	22.4 ± 0.42	19.04 ± 0.35
Glenmore II	CASS-16-12	BE41377	−43.8808091	170.3911323	1058.88	1.85	2.7	0.998795	5.2349	0.1838	1028.1	6.42 ± 0.16	15.35 ± 0.4
Glenmore II	CASS-16-13	BE41378	−43.8819129	170.3901321	1052.31	1.47	2.7	0.997492	5.4943	0.1834	1028.1	5.92 ± 0.17	13.44 ± 0.38
Glenmore II	TEK-16-31	BE41353	−44.0233496	170.4730403	746.32	1.32	2.7	0.997549	5.0841	0.1802	1027.7	5.82 ± 0.17	14.16 ± 0.4
Glenmore II	TEK-16-32	BE41354	−44.0242700	170.4797222	746.99	2.03	2.7	0.993853	5.0555	0.1811	1027.7	5.76 ± 0.14	14.16 ± 0.35
Glenmore II	TEK-16-34	BE41355	−44.0245789	170.4853663	752.97	1.31	2.7	0.999686	5.0397	0.1805	1027.7	5.62 ± 0.12	13.81 ± 0.29
Glenmore II	TEK-17-03	BE42939	−43.9924628	170.4402157	787.88	5.16	2.7	0.999857	5.0421	0.1818	1034.4	5.68 ± 0.26	14.08 ± 0.65
Glenmore II	TEK-17-04	BE42940	−43.9917690	170.4385149	785.63	1.60	2.7	0.997549	5.0152	0.1823	1034.4	5.66 ± 0.16	14.15 ± 0.39
Glenmore II	TEK-17-05	BE42941	−43.9915980	170.4380477	788.70	1.94	2.7	0.994774	5.0442	0.1828	1034.4	5.87 ± 0.15	14.62 ± 0.37
Glenmore II	TEK-17-06	BE42942	−43.9915025	170.4378310	790.14	1.77	2.7	0.987371	5.0900	0.1826	1034.4	6.08 ± 0.13	15 ± 0.34
Glenmore II	TEK-17-07	BE42943	−43.9904397	170.4362657	795.60	2.18	2.7	0.999963	5.0764	0.1836	1034.4	5.75 ± 0.11	14.31 ± 0.28
Glenmore II	TEK-17-16	BE44603	−44.0129463	170.5217036	859.18	4.38	2.7	0.999514	5.0075	0.2019	1036.2	5.63 ± 0.12	15.64 ± 0.33
Glenmore II	TEK-17-17	BE44604	−44.0129421	170.5216427	858.51	2.56	2.7	0.991640	5.1989	0.2022	1036.2	5.44 ± 0.11	14.57 ± 0.31
Glenmore II	TEK-18-02	BE44601	−44.0003398	170.5596524	867.34	1.33	2.7	0.999588	5.0337	0.2017	1036.2	5.51 ± 0.12	15.2 ± 0.32
Glenmore III	CASS-12-01	BE41373	−43.8553180	170.4150020	1204.00	1.55	2.7	0.996626	5.0356	0.1846	1028.1	8.38 ± 0.17	20.94 ± 0.43
Glenmore III	CASS-16-03	BE41375	−43.8702363	170.4018393	1124.94	0.94	2.7	0.996463	5.0883	0.1837	1028.1	7.86 ± 0.23	19.35 ± 0.56
Glenmore III	CASS-16-06	BE41376	−43.8828989	170.3882705	1045.13	2.33	2.7	0.993272	5.4872	0.1840	1028.1	7.78 ± 0.15	17.78 ± 0.35
Glenmore III	TEK-16-04	BE41356	−43.9497820	170.4025141	859.51	1.39	2.7	0.988919	5.2365	0.1821	1027.7	5.17 ± 0.12	12.34 ± 0.28
Glenmore III	TEK-16-05	BE41357	−43.9494964	170.4026375	860.77	1.69	2.7	0.994796	5.2618	0.1821	1027.7	6.37 ± 0.15	15.12 ± 0.35
Glenmore III	TEK-16-06	BE41367	−43.9252972	170.3931402	887.34	1.99	2.7	0.998032	3.9092	0.1838	1028.1	5.2 ± 0.11	16.59 ± 0.34
Glenmore III	TEK-16-07	BE41358	−43.9258101	170.3933131	885.91	1.37	2.7	0.999087	5.0855	0.1819	1027.7	6.24 ± 0.15	15.31 ± 0.37
Glenmore III	TEK-16-09	BE41368	−43.9279324	170.3938130	879.61	1.61	2.7	0.994552	5.7534	0.1832	1028.1	6.9 ± 0.15	14.96 ± 0.32

(*continued on next page*)

Table 1 (*continued*)

Landform Name	Sample ID	CAMS Laboratory number	Latitude (DD)	Longitude (DD)	Elevation (m.a.s.l.)	Sample Thickness (cm)	Density (g cm-2)	Shielding correction	Quartz weight (g)	Carrier added (g)	Carrier conc. (ppm)	10Be/9Be ± 1σ (10–14)	[10Be] ± 1σ (104) (atoms/ gram)
Glenmore III	TEK-16-17	BE41350	−44.0280620	170.4921346	744.32	2.09	2.7	0.994776	5.0922	0.1807	1027.7	5.77 ± 0.12	14.07 ± 0.3
Glenmore III	TEK-16-19	BE41351	−44.0279957	170.4916264	744.26	2.70	2.7	0.999047	5.0325	0.1802	1027.7	5.91 ± 0.15	14.52 ± 0.36
Glenmore III	TEK-16-20	BE41352	−44.0276903	170.4844973	744.87	1.62	2.7	0.999922	5.2593	0.1810	1027.7	5.91 ± 0.11	13.98 ± 0.27
Glenmore III	TEK-17-18	BE44605	−44.0110338	170.5288325	878.43	3.81	2.7	0.997930	5.2285	0.2020	1036.2	6.13 ± 0.16	16.33 ± 0.44
Glenmore III	TEK-17-27	BE42951	−43.9582592	170.5604963	1040.88	1.58	2.7	0.999623	4.2816	0.1998	1035.6	4.84 ± 0.15	15.59 ± 0.49
Glenmore III	TEK-17-28	BE42952	−43.9587300	170.5608064	1029.55	0.90	2.7	0.998421	1.8118	0.1996	1035.6	2.36 ± 0.09	17.92 ± 0.71
Glenmore III	TEK-17-29	BE42953	−43.9594415	170.5629290	994.55	1.14	2.7	0.993771	4.9555	0.2003	1035.6	6.05 ± 0.24	16.9 ± 0.67
Glenmore III	TEK-17-44	BE42956	−43.9702853	170.5749329	921.73	2.56	2.7	0.998725	5.0170	0.2006	1035.6	5.85 ± 0.14	16.16 ± 0.38
Glenmore III	TEK-17-45	BE42957	−43.9692996	170.5749512	928.01	3.21	2.7	0.998074	5.1702	0.2009	1035.6	6.46 ± 0.13	17.34 ± 0.35
Glenmore III	TEK-17-46	BE42958	−43.9657198	170.5744815	939.48	2.74	2.7	0.998290	5.0226	0.2002	1035.6	6.09 ± 0.14	16.77 ± 0.4
Glenmore III	TEK-18-01	BE44600	−44.0041507	170.5574164	856.76	1.34	2.7	0.999319	5.0309	0.2015	1036.2	5.56 ± 0.12	15.34 ± 0.32
Glenmore III	TEK-18-03	BE44602	−44.0030745	170.5592131	862.95	2.44	2.7	0.999617	5.1563	0.2017	1036.2	5.9 ± 0.12	15.91 ± 0.32
Glenmore IV	TEK-16-01	BE41346	−43.9550504	170.4036126	836.35	3.22	2.7	0.999867	5.0841	0.1808	1027.7	8.93 ± 0.17	21.8 ± 0.41
Glenmore IV	TEK-16-02	BE41347	−43.9533058	170.4036070	847.68	2.16	2.7	0.999797	5.1269	0.1801	1027.7	9.21 ± 0.17	22.22 ± 0.42
Glenmore IV	TEK-16-03	BE41348	−43.9525717	170.4017930	846.00	1.86	2.7	0.993807	5.0305	0.1800	1027.7	9.02 ± 0.22	22.17 ± 0.54
Mt John	MtJOHN-16-01	BE41360	−43.9856960	170.4630000	1008.75	2.47	2.7	0.997988	5.2129	0.1817	1027.7	7.62 ± 0.15	18.23 ± 0.37
Mt John	MtJOHN-16-02	BE41361	−43.9848282	170.4660046	1014.43	1.36	2.7	0.999019	5.7299	0.1821	1027.7	7.76 ± 0.15	16.92 ± 0.33
Mt John	MtJOHN-16-03	BE41362	−43.9846170	170.4686847	958.74	2.15	2.7	0.996682	5.2253	0.1827	1027.7	6.62 ± 0.14	15.89 ± 0.33
Mt John	MtJOHN-16-05	BE41363	−43.9806373	170.4716009	968.08	1.63	2.7	0.996990	5.0644	0.1827	1027.7	6.68 ± 0.13	16.53 ± 0.32
Mt John	MtJOHN-16-09	BE41364	−43.9722671	170.4774725	861.99	2.05	2.7	0.999720	5.0152	0.1827	1027.7	6.01 ± 0.13	15.03 ± 0.33
Mt John	MtJOHN-16-12	BE41365	−43.9716790	170.4814638	817.93	1.66	2.7	0.990621	5.0922	0.1830	1027.7	5.67 ± 0.12	13.98 ± 0.31
Mt John	MtJOHN-16-13	BE41366	−43.9670061	170.4829405	770.90	1.52	2.7	0.999524	5.1602	0.1822	1027.7	5.39 ± 0.13	13.05 ± 0.31
Erratics #1	TEK-17-47	BE42960	−43.9384955	170.5212898	731.14	3.26	2.7	0.997009	4.3912	0.2006	1035.6	4.22 ± 0.13	13.3 ± 0.43
Erratics #1	TEK-17-49	BE42961	−43.9487449	170.4964096	787.89	2.06	2.7	0.996973	5.1574	0.2001	1035.6	5.07 ± 0.12	13.58 ± 0.33
Erratics #1	TEK-17-23BR	BE44609	−43.9603837	170.5527266	786.16	1.38	2.7	0.994596	5.0640	0.2012	1036.2	5.06 ± 0.12	13.83 ± 0.33
Erratics #2	TEK-18-06	BE44612	−43.9131750	170.4321831	871.65	2.52	2.7	0.996893	5.2604	0.2017	1036.3	5.7 ± 0.12	14.98 ± 0.32
Erratics #2	TEK-18-07	BE44613	−43.9115358	170.4320676	870.26	1.93	2.7	0.999841	5.0695	0.2025	1036.3	5.56 ± 0.12	15.2 ± 0.33
Erratics #2	TEK-18-09	BE44614	−43.9079487	170.4341877	872.12	3.85	2.7	0.994688	5.1063	0.2016	1036.3	5.56 ± 0.13	15.04 ± 0.35
Erratics #2	TEK-18-11	BE44615	−43.9061253	170.4335284	875.32	4.15	2.7	0.991503	5.1089	0.2026	1036.3	5.41 ± 0.13	14.68 ± 0.37

flanking much-reduced interglacial ice bodies in the catchment headwaters (Fig. 2). The dating work targeted localities with particularly well-preserved representations of the moraine sequence. Results of the dating are detailed in Table 3. Samples marked by a single asterisk (*) next to the sample ID are considered outliers and are not included in the mean age calculations for each component of the glacial sequence as set out in Table 4. Probability density functions (i.e. "camelplots") in Fig. 4 give visual representations of age populations of the glacial landforms. The mean age results are expressed as the number of samples (*n*) excluding outliers, the arithmetic mean ± standard-error, and the external error in parentheses. Overall, the mapping and dating provides a basis for subdividing the landform sequence into five main chronometric elements, identified here as Last Glacial, deglacial, late glacial, early Holocene and Holocene (Table 4). These are described and discussed in the sections below. A geomorphological profile of the Takapō/Tekapo and Cass valleys (Fig. 5) illustrates the relative positions and ages of the moraine sequences, in relation to similar profiles for the Pukaki and Ohau valleys from Denton et al. (2021).

4.1. *Last glacial moraine sequence*

The Last Glacial landforms were produced when the glacier was in a close to fully expanded extent (full glacial) in the Takapō/Tekapo valley, indicative of maximal glacial climatic conditions. Four components to the Last Glacial sequence have been identified, from older to younger the Glenmore IV, Glenmore III, Glenmore II, and Glenmore I moraine belts. An additional aspect comprises erratic boulders on the Mt John ice-molded bedrock knob deposited during downwasting of the ice surface.

The Glenmore IV landform unit comprises an isolated remnant of lateral moraine in the southwestern part of the moraine complex. This ridge has a notably subdued surface form compared to all adjacent inboard moraines, which led Barrell et al. (2011) to interpret the moraine ridge as early Last Glacial age. Three boulders sampled from the ridge returned tightly clustered ages ranging from 27,400 ± 670 yrs to 27,270 ± 510 yrs and mean age of 27,330 ± 40 (550) (1σ = 60) yrs [*n* = 3]. These results show the Barrell et al. (2011) age interpretation is incorrect and the Glenmore IV moraine ridge was instead formed during the latter part of the Last Glacial and is coeval with the ~27 kyr moraine belt extensively preserved in the adjacent Pukaki valley (Kelley et al., 2014; Doughty et al., 2015; Strand et al., 2019; Denton et al., 2021).

The Glenmore III belt of moraine ridges and till plains is as much as several hundred meters wide and extends fairly continuously around the periphery of the Last Glacial moraine complex of the Takapō/Tekapo valley. The ground of this moraine belt includes topographic lineaments interpreted as flutes (Barrell et al., 2011) and in some cases paleo-crevasse fills (Sutherland et al., 2019b). Notably near the Lake Takapō/Tekapo outlet, aerial imagery reveals a till sheet of the Glenmore III belt superimposed on an underlying braided outwash plain. This indicates that this moraine belt records an advance of the ice front from a more inboard position. Twenty samples returned ages ranging from 20,310 ± 410 yrs to 15,300 ± 350 yrs. Two ages, 15,300 ± 350 yrs (TEK-16-04) and 16,530 ± 520 yrs (TEK-17-27) are considered outliers due to being younger than most ages from the next inboard moraine belt (Glenmore II). The remaining eighteen samples afforded a mean age of 19,160 ± 140 (410) (1σ = 590) yrs.

The Glenmore II moraine belt is a relatively broad area of moraine ridges and hummocky moraine. Its relation to the outboard Glenmore III belt is best expressed in right-lateral moraines where the Cass valley glacier merged into the main Takapō/Tekapo glacier (Fig. 6). Ages from twenty-one samples collected from the Glenmore II moraine belt range from 19,680 ± 440 yrs to 14,200 ± 400 yrs and form an approximately normal distribution. Two ages, 14,200 ± 400 yrs (CASS-16-12) and 16,210 ± 420 yrs (CASS-16-13), are treated as outliers because they are inconsistently young compared to most ages from the inboard Glenmore I moraine belt. With the two outliers removed, the remaining nineteen samples afford a mean age of 18,870 ± 90 (390) (1σ = 410) yrs.

The Glenmore I moraine comprises arrays of semicontinuous moraine ridges and hummocky moraine, with areas of terrain that is in places notably fluted (Barrell et al., 2011, 2013; Sutherland et al., 2019b). The Glenmore I moraine, and the deglacial moraines (see below) are part of the Tekapo glacial landform set, whereas the Glenmore IV-II moraines are part of the Mt John landform set (Fig. 2). For the most part, no prominent outwash plains issue from the Glenmore I moraine belt, suggesting the moraine belt formed during a time of general ice wasting and recession. Thirteen samples yielded ages ranging from 19,240 ± 450 yrs to 16,960 ± 400 yrs with an approximately normal distribution. Two samples yielded ages of 19,240 ± 450 yrs (TEK-17-11) and 19,110 ± 380 yrs (TEK-17-15) and are considered outliers due to their being older than most ages from the outboard Glenmore II moraine. One additional age, 16,960 ± 400 yrs (TEK-17-21), is identified as an outlier based on Peirce's Criterion. With three outliers removed, the remaining ten samples afford a mean age of 18,030 ± 100 (370) (1σ = 310) yrs.

Scattered glacial erratic boulders deposited on the up-flow (stoss) side of the Mt John ice-molded bedrock hill afforded ages ranging from 19,910 ± 410 yrs to 17,210 ± 410 yrs (Fig. 7). The boulders are spread over an altitudinal range of ~220 m and are interpreted to have been deposited during recession of the Takapō/Tekapo glacier. Based on the overall distribution of ages, it is likely that the oldest and youngest ages are outliers, and the remaining 6 ages form a tight cluster in the range of 18,260 ± 360 and 17,770 ± 440 yrs. Collectively, they indicate notable downwasting of the glacier at ~18 ka, approximating the ice withdrawal from the Glenmore II to the Glenmore I moraine belts. Because the boulders record progressive emergence of land from beneath ice rather than an isochronous landform like a single moraine ridge, we have not calculated a mean age (see Fig. 12).

4.2. *Deglacial and late glacial moraines in the cass valley*

In this study, we tracked the deglaciation up the Cass valley to localized well-preserved moraine sequences in the catchment headwaters (Figs. 2 and 5). Farthest down-valley are remnants of left-lateral moraines (Fig. 8). The outer ridge (Cass II) returned an age of 17,370 ± 290 (450) (1σ = 580) yrs (*n* = 4) while the inner moraine (Cass I) afforded an age of 16,350 ± 120 (350) (1σ = 170) yrs (*n* = 2).

In the Ailsa valley, a left lateral moraine complex of deglacial age with four distinguishable ridges (Ailsa VI-III) is abutted by two parallel moraine ridges (Ailsa II-I) of late-glacial age (Figs. 8 and 9). Mean landform ages of the deglacial moraine ridges are 16,950 ± 340 (480) (1σ = 480) yrs (Ailsa VI; *n* = 2), 16,930 ± 130 (360) (1σ = 460) yrs (Ailsa V; *n* = 5), 16,620 ± 280 (440) (1σ = 490) yrs (Ailsa IV; *n* = 3), and 16,860 ± 190 (390) (1σ = 270) yrs (Ailsa III; *n* = 2). Mean landform ages of the late-glacial moraines are 13,550 ± 160 (320) (1σ = 440) yrs (Ailsa II; *n* = 7) and 12,910 ± 110 (280) (1σ = 190) yrs (Ailsa I; *n* = 3) (Table 3). In the Lucia valley, deglacial and late-glacial moraines are preserved on the right lateral margin of the hanging valley, outboard of the Holocene moraine sequence (Figs. 10 and 11), with respective ages of 16,790 ± 130 (360) (1σ = 300) yrs (Lucia XIV; *n* = 5) and 13,290 ± 70 (280) (1σ = 140) yrs (Lucia XIII; *n* = 4) (Table 3).

Altogether, 23 ages from multiple deglacial moraine remnants in the Cass valley headwaters range from 18,030 ± 530 yrs to 16,230 ± 310 yrs with no identified outliers, affording an overall mean age of 16,930 ± 100 (350) (1σ = 490) yrs. Fourteen ages from the late-glacial moraine ridges range from 14,030 ± 270 yrs to 12,720 ± 240 yrs, with no identified outliers and an overall mean age of 13,340 ± 110 (290) (1σ = 400) yrs. There are two notable geometric considerations. First is that the Cass II-I moraine remnant has a relatively steep gradient, which aligns tolerably well with the position and elevation of the Ailsa and Lucia deglacial moraines (Fig. 5). Second, the Alisa and Lucia late-glacial moraines closely parallel the deglacial moraines, indicating that they were formed by glacier tongues closely similar to the deglacial

Table 2
^{10}Be blank details.

Blank no.	CAMS laboratory no.	Sample ID	Corresponding Samples	Be Carrier Name	Carrier added (g)	Carrier conc. (ppm)	^{10}Be/^{9}Be ± 1σ (10^{-16})	N [^{10}Be] ± 1σ (10^{3} atoms)	Average ^{9}Be current (μA) (runs)
1	BE28279	Blank_2_2009Oct13	LUC-09-13, 16	LDEO carrier 4	0.1630	996	12.06 ± 2.43	13.09 ± 2.63	17.2 (2)
2	BE28273	Blank_3_2009Oct16	LUC-09-23, 24, 26, 27, 30	LDEO carrier 4	0.1815	996	11.58 ± 1.84	18.03 ± 2.22	18.4 (4)
3	BE28932	Blank_1_2010Jan22	LUC-09-01, 02, 03, 44, 05, 42	LDEO carrier 4	0.1844	996	11.58 ± 2.06	14.27 ± 2.54	20.1 (2
4	BE28849	Blank_1_2010Mar05	LUC-09-04, 08, 47	LDEO carrier 5	0.1820	1024	11.20 ± 1.85	13.95 ± 2.31	23.7 (2)
5	BE28877	Blank_1_2010Apr02	LUC-09-10, 17, 18, 31, 35, 38, 41, 49	LDEO carrier 5	0.1828	1025	23.91 ± 2.85	29.93 ± 3.47	15.3 (3)
6	BE29513	Blank_1_2010Apr29	LUC-09-48, 37	LDEO carrier 5	0.1822	1026	17.33 ± 2.86	21.64 ± 2.93	17.6 (3)
7	BE29484	Blank_1_2010Jun22	LUC-09-20, 22	LDEO carrier 5	0.1511	1026	12.74 ± 2.05	13.20 ± 2.12	17.0 (3)
8	BE29488	Blank_2_2010Jun22	LUC-09-15	LDEO carrier 5	0.1502	1026	17.33 ± 2.88	39.22 ± 3.56	17.7 (3)
9	BE40245	Blank_1_2015Nov12	LUC-09-06, 07, 09, 11, 12, 21; CASS-14-04, 05, 06	LDEO carrier 5	0.1830	1043	5.75 ± 1.59	7.34 ± 2.03	17.1 (2)
10	BE40025	Blank_1_2015Oct28	CASS-12-07, 08, 09, 10, 11, 12, 13; CASS-14-01, 02, 03	LDEO carrier 5	0.1836	1043	3.41 ± 1.65	4.37 ± 2.12	11.3 (3)
11	BE41349	Blank_1_2016May18	TEK-16-01, 02, 03, 17, 19, 20, 31, 32, 34	LDEO carrier 6	0.1795	1028	0.00 ± 0.00	0.00 ± 0.00	24.0 (2)
12	BE41359	Blank_1_2016May26	TEK-16-04, 05, 07; MtJOHN-16-01, 02, 03, 05, 09, 12, 13	LDEO carrier 6	0.1818	1028	0.47 ± 1.63	0.59 ± 2.03	24.8 (2)
13	BE41372	Blank_1_2016Jun06	TEK-16-06, 09, 12, 13, 16; CASS-12-01, 04; CASS-16-03, 06, 12, 13	LDEO carrier 6	0.1885	1028	5.95 ± 1.57	7.49 ± 1.98	20.6 (2)
14	BE42948	Blank_1_2017May01	TEK-17-03, 04, 05, 06, 07, 13, 14, 15, 25	LDEO carrier 6	0.1831	1034	2.86 ± 1.94	3.61 ± 2.45	21.7 (2)
15	BE42959	Blank_1_2017May09	TEK-17-27, 28, 29, 44, 45, 46, 47, 49	LDEO carrier 6	0.2072	1036	0.88 ± 2.21	1.22 ± 3.07	18.5 (2)
16	BE42968	Blank_1_2017May15	CASS-17-06, 09, 13, 14, 15, 16, 22, 23, 26, 30, 32	LDEO carrier 6	0.2101	1036	2.20 ± 1.99	3.09 ± 2.79	23.0 (2)
17	BE44606	Blank_1_2018Apr23	TEK-18-01, 02, 03; TEK-17-16, 17, 18, 11, 12, 23	LDEO carrier 6	0.2028	1036	2.78 ± 0.98	3.90 ± 1.38	24.9 (2)
18	BE44616	Blank_1_2018May02	TEK-18-04, 05, 06, 07, 09, 11; TEK-17-20, 21, 22	LDEO carrier 6	0.2025	1036	6.03 ± 1.51	8.45 ± 2.11	23.1 (2)
19	BE44837	Blank_1_2018May11	CASS-17-11, 18, 19, 20, 27, 28, 29, 31, 33, 35, 36	LDEO carrier 6	0.2092	1037	5.98 ± 1.68	8.36 ± 2.35	20.8 (2)

configuration. Overall, these observations suggest that by ~17 ka, the glacier in the Cass valley headwaters had achieved an equilibrium condition that was maintained, or reattained, over sufficient time for several moraine ridges to form. That glacier extent was only slightly larger than it was at late-glacial time.

4.3. Holocene moraines

The Lucia valley has a well-preserved sequence of concentric Holocene moraine ridges, and we were able to obtain exposure ages from twelve of the ridges (Figs. 10 and 11). The mean ages are 11,790 ± 250 (340) (1σ = 500) yrs (Lucia XII; *n* = 4), 11,200 ± 120 (250) (1σ = 170) yrs (Lucia IX; *n* = 2), 11,290 ± 170 (280) (1σ = 290) yrs (Lucia VIII; *n* = 2), 9690 ± 110 (250) (1σ = 160) yrs (Lucia VI; *n* = 2), 9960 ± 590 (620) (1σ = 840) yrs (Lucia V; *n* = 2), 8600 ± 230 (290) (1σ = 330) yrs (Lucia IV; *n* = 2), 8340 ± 150 (220) (1σ = 210) yrs (Lucia III; *n* = 2), 1225 ± 30 (40) (1σ = 50) yrs (Lucia II; *n* = 2), and 300 ± 110 (110) (1σ = 160) yrs (Lucia I; *n* = 3, −1 outlier).

4.4. ELA estimation

ELA estimates for paleo-glacier extents in the Cass valley are given in Table 5. Our Cass valley ΔELA estimates are referenced to the Ridge Glacier (Fig. 2), one of 51 Southern Alps index glaciers where annual glacier ELAs have been recorded since C.E. 1978 using oblique aerial photography (Chinn, 1995; Chinn et al., 2005, 2012; Clare et al., 2002; Lorrey et al., 2022). The Ridge Glacier is only ~3 km from the Lucia valley where the deglacial to Holocene ELAs are estimated, and we use its "steady-state" ELA of 2260 m a.s.l. as our "modern" snowline benchmark (Chinn, 1995). As described in the Methods section, a change in the configuration of the Lucia valley ice catchment at the start of the Holocene (Figs. 10 and 11) led us to determine an adjustment for the MELM-based Holocene ELAs. We consider this makes for a more valid comparison with the more full-bodied, valley-filling glacier that characterized the deglacial, and the termination through to late-glacial time.

By ~17 ka, the glacier in the Cass valley headwaters had achieved an equilibrium condition as defined by the right-lateral moraine that has a maximum elevation of 1765 m a.s.l. In the Lucia valley, the ELA became progressively higher through the late glacial and the Holocene. Earliest Holocene (~11.5 kyr) ELA was ~35 m higher than the ~13 kyr ELA, with further sequential rise in ELA totaling ~175 m through to ~0.3 kyr ago, as registered by the valley's youngest moraine. This mirrors the pattern of Holocene snowline changes documented elsewhere in the Southern Alps (Kaplan et al., 2010; Putnam et al., 2012; Doughty et al., 2013). We note that in New Zealand, the full glacial-to-interglacial ELA rise includes a considerable Holocene component (Kaplan et al., 2010; Putnam et al., 2012; Doughty et al., 2013), which is not necessarily the case for other glacier systems around the globe.

More challenging for this study was obtaining an ELA estimate that is representative of full glacial conditions. The prominent right-lateral moraine along the lower Cass valley has a well-defined MELM of

Table 3
^{10}Be surface-exposure ages (in thousands of cal. yrs before AD 2020; ± 1σ) from the Takapō/Tekapo catchment moraines. Ages are calculated using the Putnam et al. (2010) Macaulay production rate, according to time-independent scaling ('St') and time-dependent scaling ('Lm') as described in the Methods section; 'Lm' ages (bold) are discussed in the text. Outlier ages are marked by an asterisk (*) next to the sample ID.

Landform	Sample ID	St age (kyrs)	Lm age (kyrs)
Lucia I	LUC-09-13	0.43 ± 0.01	**0.40 ± 0.01**
Lucia I	LUC-09-15*	2.91 ± 0.05	**2.97 ± 0.05**
Lucia I	LUC-09-16	0.20 ± 0.08	**0.19 ± 0.07**
Lucia II	LUC-09-20	1.15 ± 0.07	**1.18 ± 0.07**
Lucia II	LUC-09-21	1.25 ± 0.04	**1.27 ± 0.04**
Lucia II	LUC-09-22	1.20 ± 0.06	**1.23 ± 0.06**
Lucia III	LUC-09-23	8.58 ± 0.14	**8.49 ± 0.14**
Lucia III	LUC-09-24	8.28 ± 0.33	**8.19 ± 0.32**
Lucia IV	LUC-09-26	8.46 ± 0.15	**8.37 ± 0.15**
Lucia IV	LUC-09-27	8.92 ± 0.15	**8.83 ± 0.14**
Lucia V	LUC-09-17	9.45 ± 0.13	**9.37 ± 0.13**
Lucia V	LUC-09-18	10.62 ± 0.14	**10.55 ± 0.14**
Lucia VI	LUC-09-30	9.88 ± 0.16	**9.81 ± 0.16**
Lucia VI	LUC-09-31	9.66 ± 0.20	**9.58 ± 0.19**
Lucia VII	LUC-09-35	11.49 ± 0.16	**11.43 ± 0.16**
Lucia VIII	LUC-09-37	11.51 ± 0.16	**11.45 ± 0.16**
Lucia VIII	LUC-09-38	11.52 ± 0.16	**11.46 ± 0.16**
Lucia VIII	LUC-09-41	11.01 ± 0.19	**10.95 ± 0.19**
Lucia IX	LUC-09-42	11.14 ± 0.28	**11.09 ± 0.28**
Lucia IX	LUC-09-44	11.38 ± 0.18	**11.32 ± 0.18**
Lucia X	LUC-09-48*	12.25 ± 0.20	**12.17 ± 0.20**
Lucia XI	LUC-09-49	10.99 ± 0.19	**10.94 ± 0.19**
Lucia XII	LUC-09-10	12.27 ± 0.20	**12.19 ± 0.20**
Lucia XII	LUC-09-11	11.43 ± 0.22	**11.37 ± 0.21**
Lucia XII	LUC-09-12	12.34 ± 0.25	**12.27 ± 0.25**
Lucia XII	LUC-09-47	11.41 ± 0.31	**11.35 ± 0.31**
Lucia XIII	LUC-09-06	13.42 ± 0.31	**13.32 ± 0.31**
Lucia XIII	LUC-09-07	13.57 ± 0.26	**13.47 ± 0.25**
Lucia XIII	LUC-09-08	13.34 ± 0.20	**13.24 ± 0.20**
Lucia XIII	LUC-09-09	13.23 ± 0.25	**13.13 ± 0.25**
Lucia XIV	LUC-09-01	16.70 ± 0.22	**16.48 ± 0.22**
Lucia XIV	LUC-09-02	16.72 ± 0.29	**16.51 ± 0.28**
Lucia XIV	LUC-09-03	17.43 ± 0.40	**17.18 ± 0.39**
Lucia XIV	LUC-09-04	17.08 ± 0.20	**16.85 ± 0.20**
Lucia XIV	LUC-09-05	17.17 ± 0.26	**16.94 ± 0.26**
Ailsa I	CASS-17-33	13.16 ± 0.30	**13.10 ± 0.30**
Ailsa I	CASS-17-35	12.79 ± 0.24	**12.72 ± 0.24**
Ailsa I	CASS-17-36	12.97 ± 0.25	**12.91 ± 0.24**
Ailsa II	CASS-17-26	13.67 ± 0.29	**13.60 ± 0.29**
Ailsa II	CASS-17-27	13.40 ± 0.29	**13.34 ± 0.29**
Ailsa II	CASS-17-28	13.15 ± 0.28	**13.08 ± 0.28**
Ailsa II	CASS-17-29	13.28 ± 0.25	**13.21 ± 0.25**
Ailsa II	CASS-17-30	14.31 ± 0.33	**14.22 ± 0.33**
Ailsa II	CASS-17-31	13.43 ± 0.26	**13.37 ± 0.26**
Ailsa II	CASS-17-32	14.10 ± 0.27	**14.03 ± 0.27**
Ailsa III	CASS-17-22	16.85 ± 0.32	**16.67 ± 0.32**
Ailsa III	CASS-17-23	17.25 ± 0.35	**17.05 ± 0.35**
Ailsa IV	CASS-17-18	17.37 ± 0.34	**17.18 ± 0.33**
Ailsa IV	CASS-17-19	16.44 ± 0.32	**16.29 ± 0.31**
Ailsa IV	CASS-17-20	16.54 ± 0.29	**16.39 ± 0.29**
Ailsa V	CASS-17-11	16.98 ± 0.33	**16.82 ± 0.32**
Ailsa V	CASS-17-13	17.10 ± 0.32	**16.93 ± 0.32**
Ailsa V	CASS-17-14	17.28 ± 0.33	**17.10 ± 0.33**
Ailsa V	CASS-17-15	17.02 ± 0.32	**16.85 ± 0.32**
Ailsa V	CASS-17-16	18.26 ± 0.53	**18.03 ± 0.53**
Ailsa VI	CASS-17-06	17.49 ± 0.33	**17.28 ± 0.33**
Ailsa VI	CASS-17-09	16.79 ± 0.41	**16.61 ± 0.40**
Cass I	CASS-14-05	16.35 ± 0.31	**16.23 ± 0.31**
Cass I	CASS-14-06	16.60 ± 0.43	**16.47 ± 0.43**
Cass II	CASS-14-01	17.52 ± 0.33	**17.37 ± 0.33**
Cass II	CASS-14-02	17.98 ± 0.57	**17.81 ± 0.57**
Cass II	CASS-14-03	17.92 ± 0.34	**17.75 ± 0.33**
Cass II	CASS-14-04	16.67 ± 0.32	**16.54 ± 0.31**
Glenmore I	TEK-16-12	17.89 ± 0.36	**17.78 ± 0.35**
Glenmore I	TEK-16-13	17.93 ± 0.35	**17.83 ± 0.35**
Glenmore I	TEK-16-16	18.11 ± 0.41	**18.00 ± 0.41**
Glenmore I	TEK-17-11*	19.38 ± 0.45	**19.24 ± 0.45**
Glenmore I	TEK-17-12	18.60 ± 0.56	**18.48 ± 0.56**
Glenmore I	TEK-17-13	17.73 ± 0.43	**17.64 ± 0.43**
Glenmore I	TEK-17-14	18.42 ± 0.68	**18.31 ± 0.67**
Glenmore I	TEK-17-15*	19.25 ± 0.39	**19.11 ± 0.38**
Glenmore I	TEK-17-20	18.51 ± 0.57	**18.40 ± 0.57**
Glenmore I	TEK-17-21*	17.03 ± 0.44	**16.96 ± 0.43**
Glenmore I	TEK-17-22	18.32 ± 0.46	**18.21 ± 0.46**
Glenmore I	TEK-18-04	17.72 ± 0.41	**17.64 ± 0.41**
Glenmore I	TEK-18-05	18.12 ± 0.47	**18.03 ± 0.47**
Glenmore II	CASS-12-04	18.99 ± 0.58	**18.76 ± 0.57**
Glenmore II	CASS-12-07	18.63 ± 0.35	**18.45 ± 0.35**
Glenmore II	CASS-12-08	19.33 ± 0.36	**19.11 ± 0.36**
Glenmore II	CASS-12-09	18.87 ± 0.35	**18.68 ± 0.35**
Glenmore II	CASS-12-10	19.54 ± 0.37	**19.32 ± 0.36**
Glenmore II	CASS-12-11	19.12 ± 0.36	**18.92 ± 0.36**
Glenmore II	CASS-12-12	19.16 ± 0.36	**18.95 ± 0.36**
Glenmore II	CASS-12-13	19.31 ± 0.36	**19.10 ± 0.36**
Glenmore II	CASS-16-12*	16.21 ± 0.42	**16.11 ± 0.42**
Glenmore II	CASS-16-13*	14.24 ± 0.41	**14.20 ± 0.40**
Glenmore II	TEK-16-31	19.13 ± 0.55	**19.01 ± 0.55**
Glenmore II	TEK-16-32	19.29 ± 0.48	**19.17 ± 0.48**
Glenmore II	TEK-16-34	18.51 ± 0.40	**18.41 ± 0.39**
Glenmore II	TEK-17-03	18.88 ± 0.88	**18.76 ± 0.88**
Glenmore II	TEK-17-04	18.56 ± 0.52	**18.45 ± 0.52**
Glenmore II	TEK-17-05	19.24 ± 0.48	**19.10 ± 0.48**
Glenmore II	TEK-17-06	19.83 ± 0.45	**19.68 ± 0.44**
Glenmore II	TEK-17-07	18.65 ± 0.37	**18.54 ± 0.37**
Glenmore II	TEK-17-16	19.69 ± 0.41	**19.52 ± 0.41**
Glenmore II	TEK-17-17	18.24 ± 0.39	**18.12 ± 0.38**
Glenmore II	TEK-18-02	18.58 ± 0.40	**18.46 ± 0.39**
Glenmore III	CASS-12-01	19.77 ± 0.41	**19.53 ± 0.40**
Glenmore III	CASS-16-03	19.33 ± 0.57	**19.12 ± 0.56**
Glenmore III	CASS-16-06	19.16 ± 0.38	**18.97 ± 0.38**
Glenmore III	TEK-16-04*	15.34 ± 0.35	**15.30 ± 0.35**
Glenmore III	TEK-16-05	18.74 ± 0.43	**18.61 ± 0.43**
Glenmore III	TEK-16-06	20.12 ± 0.42	**19.93 ± 0.42**
Glenmore III	TEK-16-07	18.48 ± 0.45	**18.35 ± 0.45**
Glenmore III	TEK-16-09	18.25 ± 0.39	**18.13 ± 0.39**
Glenmore III	TEK-16-17	19.20 ± 0.41	**19.08 ± 0.41**
Glenmore III	TEK-16-19	19.83 ± 0.50	**19.69 ± 0.49**
Glenmore III	TEK-16-20	18.90 ± 0.37	**18.79 ± 0.37**
Glenmore III	TEK-17-18	20.19 ± 0.54	**20.00 ± 0.54**
Glenmore III	TEK-17-27*	16.63 ± 0.53	**16.53 ± 0.52**
Glenmore III	TEK-17-28	19.22 ± 0.76	**19.04 ± 0.76**
Glenmore III	TEK-17-29	18.75 ± 0.75	**18.59 ± 0.74**
Glenmore III	TEK-17-44	19.12 ± 0.45	**18.96 ± 0.45**
Glenmore III	TEK-17-45	20.52 ± 0.42	**20.31 ± 0.41**
Glenmore III	TEK-17-46	19.59 ± 0.47	**19.42 ± 0.47**
Glenmore III	TEK-18-01	18.92 ± 0.40	**18.79 ± 0.40**
Glenmore III	TEK-18-03	19.69 ± 0.40	**19.53 ± 0.40**
Glenmore IV	TEK-16-01	27.79 ± 0.52	**27.27 ± 0.51**
Glenmore IV	TEK-16-02	27.85 ± 0.52	**27.32 ± 0.51**
Glenmore IV	TEK-16-03	27.93 ± 0.68	**27.40 ± 0.67**
Mt John	MtJOHN-16-01	20.12 ± 0.41	**19.91 ± 0.41**
Mt John	MtJOHN-16-02	18.41 ± 0.36	**18.26 ± 0.36**
Mt John	MtJOHN-16-03	18.22 ± 0.38	**18.09 ± 0.38**
Mt John	MtJOHN-16-05	18.74 ± 0.37	**18.58 ± 0.36**
Mt John	MtJOHN-16-09	18.56 ± 0.40	**18.44 ± 0.40**
Mt John	MtJOHN-16-12	17.99 ± 0.40	**17.89 ± 0.39**
Mt John	MtJOHN-16-13	17.28 ± 0.41	**17.21 ± 0.41**
Erratics #1	TEK-17-23	18.16 ± 0.43	**18.06 ± 0.43**
Erratics #1	TEK-17-47	18.49 ± 0.60	**18.39 ± 0.60**
Erratics #1	TEK-17-49	17.86 ± 0.44	**17.77 ± 0.44**
Erratics #2	TEK-18-06	18.49 ± 0.39	**18.36 ± 0.39**
Erratics #2	TEK-18-07	18.64 ± 0.41	**18.51 ± 0.41**
Erratics #2	TEK-18-09	18.78 ± 0.44	**18.64 ± 0.44**
Erratics #2	TEK-18-11	18.38 ± 0.46	**18.26 ± 0.46**

1340 m a.s.l. (Fig. 6). However, the abrupt up-valley end of this moraine suggests that its upstream limit is not a depositional feature, but rather a truncation by erosion, or non-deposition due to influent Last Glacial ice flow from cirques on the western flank of the catchment, and we therefore take 1340 m a.s.l. as a minimum constraint on full-glacial ELA for the Cass valley. Determination of more precise ELA constraint is complicated by the valley's size and complexity. In addition, the south-draining Cass valley obliquely crosses the northwest-southeast

Table 4
Summary statistics for Takapō/Tekapo moraine ^{10}Be surface-exposure age distributions.

Landform Name	*N total (N excl.)*	Mean Age (yrs)	±	SEM (yrs)	Ext. Unc. (yrs)	1σ (yrs)
Holocene:						
Lucia I	3 (1 excl.)	**300**	±	**110**	**110**	160
Lucia II	3	**1225**	±	**30**	**40**	50
Lucia III	2	**8340**	±	**150**	**220**	210
Lucia IV	2	**8600**	±	**230**	**290**	330
Lucia V	2	**9960**	±	**590**	**620**	840
Lucia VI	2	**9690**	±	**110**	**220**	160
Early Holocene:						
All Early Holocene Ages	*12*	***11,500***	±	**130**	***270***	*470*
Lucia VIII	3	**11,290**	±	**170**	**280**	290
Lucia IX	2	**11,200**	±	**120**	**250**	170
Lucia XII	4	**11,790**	±	**250**	**340**	500
Late Glacial:						
All Late Glacial Ages	*14*	***13,340***	±	***110***	***290***	*400*
Ailsa I	3	**12,910**	±	**110**	**280**	190
Lucia XIII	4	**13,290**	±	**70**	**280**	140
Ailsa II	7	**13,550**	±	**160**	**320**	430
Deglacial:						
All Deglacial Ages	*23*	***16,930***	±	***100***	***350***	*490*
Lucia XIV	5	**16,790**	±	**130**	**360**	300
Ailsa III	2	**16,860**	±	**190**	**390**	270
Ailsa IV	3	**16,620**	±	**280**	**440**	490
Ailsa V	5	**16,930**	±	**130**	**360**	460
Ailsa VI	2	**16,950**	±	**340**	**480**	480
Cass I	2	**16,350**	±	**120**	**350**	170
Cass II	4	**17,370**	±	**290**	**450**	580
Last Glacial:						
Glenmore I	13 (3 excl.)	**18,030**	±	**100**	**370**	310
Glenmore II	21 (2 excl.)	**18,870**	±	**90**	**390**	410
Glenmore III	20 (2 excl.)	**19,160**	±	**140**	**410**	590
Glenmore IV	3	**27,330**	±	**40**	**550**	60

orographically-induced ELA gradient across the Southern Alps that is prominent under modern interglacial climate (e.g. Porter, 1975; Chinn, 1995). A similar ELA gradient likely existed under glacial climate, with associated spatial contrasts in ELA for accumulation areas around the flanks and head of the glaciated Cass catchment (Golledge et al., 2012). As a first approximation, we adopt the mid-point of the ~50 km long Cass Glacier profile as the position of the ELA on the glacier trunk. The mid-point (i.e. at ~25 km profile distance) lies ~1 km up-valley of the end of the lower Cass lateral moraines (Fig. 5). The lateral moraine has a well-resolved gradient of ~100 m rise per ~2.5 km distance, and extrapolating its gradient ~1 km up-valley indicates a glacier surface elevation of ~1385 m at the valley mid-point. We take this as a working estimate of the Last Glacial ELA of the Cass Glacier. It is 875 m lower than the estimated modern ELA defined at Ridge Glacier (Table 5). In addition, this Last Glacial ELA estimate is corroborated by the glacier modeling of Golledge et al. (2012), which incorporated reanalysis-based climatological information that accounts for the aforementioned topo-climatic gradients in the Southern Alps. Numerical glaciological modeling by Golledge et al. (2012) indicates an ELA over the middle part of the Cass valley of between ~800 and ~900 m lower than modern, which is compatible with our MELM-extrapolated estimate.

4.5. Glacier-inferred temperature estimates

In the Cass valley, we converted the MELM-based estimates of paleo-ELAs into temperature changes relative to modern values (as determined from the nearby Ridge Glacier, see Methods section and Table 5) by applying a lapse rate of 5 °C km^{-1} (Norton, 1985; Anderson et al., 2010; Golledge et al., 2012; Doughty et al., 2013; Eaves et al., 2017). Using this approach, we calculate that the glacial configuration ~17 kyrs ago represents a mean annual air temperature change ~2.5 °C cooler than modern, while the late-glacial, early Holocene, and pre-industrial glacier configurations equate to temperatures ~2.2 °C, ~2.0 °C, ~1.1 °C cooler than modern (Table 5). For our full glacial temperature estimate, we turn to the Golledge et al. (2012) to avoid the complexities of comparing ΔELA values across the steep ELA gradient of the Southern Alps. Golledge et al. (2012) demonstrated that the modeled Southern Alps ice-field achieved best fit with mapped Last Glacial terminal ice limits with a mean annual air temperature 6.25 ± 0.25 °C cooler and 25% less mean annual precipitation than modern (based on 30-year mean-annual air temperature and mean-annual precipitation data from C.E. 1951 - 1980) (Table 5). The marked contrast between the Golledge et al. (2012) Last Glacial temperature estimate and our ~17 ka estimate indicates temperature warming of ~3.75 °C between ~18 and ~17 kyrs ago (Table 5). The climate of ~17 kyrs ago also approximates climatic conditions that prevailed at ~16 kyrs and ~13 kyrs ago, as there is a ~16 kyr deglacial moraine in the upper Cass valley, and late-glacial moraines in the Ailsa and Lucia valleys proximal to the ~17 kyr old deglacial moraines. In the Cass valley, there is no geomorphic record of ice extent (i.e. moraines) between ~16 and ~13 kyrs ago, indicating that climatic conditions during that interval were similar to or warmer than was the case at ~17 and ~13 kyrs ago. Thus, our estimates for the pace and magnitude of paleo-ELA change during that part of the last glacial termination are minimum values. Further work involving whole-catchment-glaciological modeling of the combined Takapō/Tekapo and Cass valleys, akin to that done in some other Southern Alps valleys (e.g., Putnam et al., 2013a; Eaves et al., 2017; Koffman et al., 2017), may help evaluate hypotheses of transient climate conditions and glacier extents/geometries, particularly during the transition from full-glacial to late-glacial climate. Altogether, our results indicate that the climate transition from Last Glacial to early Holocene in New Zealand involved mean annual air temperatures becoming ~4.3 ± 0.5 °C warmer, with ~90% of the warming taking place between ~18,000 and ~17,000 yrs ago.

5. Discussion

Sustained retreat of the Takapō/Tekapo glacier from its full-glacial positions began ~18 kyrs ago, following relatively minor recession after it attained its maximum full-glacial extent ~19 kyrs ago. By ~17 kyrs ago, ice had retreated hugely, with the Cass glacier reestablishing in the upper reaches of its catchment, much closer to interglacial moraines than full glacial moraines (Fig. 5). This indicates that in no more than ~1000 years, the regional climate had achieved nearly interglacial conditions, with mean annual air temperature ~3.8 °C warmer than at 18 kyrs.

An often-posed question is whether the formation of post-glacial lakes played a role in accelerating ice retreat during the last termination (Sutherland et al., 2020). In relation to our study area, an important factor that informs this issue is a broad ridge of glaciogenic sediments in the Takapō/Tekapo Last Glacial moraine complex that runs transverse to the Cass valley mouth, and through which the Cass River has cut a

Table 5
Paleo-glacier ELA and derived temperature estimates. Paleo-glacier ELA values (meters above sea level – m a.s.l.) were determined from GPS elevation measurements of moraines (using the MELM method, see Methods section), with the exception of the Modern ELA value (*) which uses the "steady state" ELA of the Ridge Glacier (Chinn, 1995), and full-glacial ELA and temperature (temp) values (°) based on MELM extrapolation and a 5 °C/km lapse rate applied in the numerical glaciological modeling of Golledge et al. (2012). Deglacial to modern temperature change values also use a 5 °C/km lapse rate. See text for explanation of Adjusted ELA values for Early Holocene to Pre-Industrial moraines.

Age (kyrs)	Landform group	MELM (m a.s.l.)	ELA estimate (m a.s.l.)	Adjusted ELA (m a.s.l.)	ELA relative to "Modern" (m)	ELA rise from LGM (m)	Temp change relative to Modern (°C)	Temp change from Last Glacial (°C)	% Temp change (Last Glacial to Modern)	% Temp change during deglaciation (Last Glacial to Early Holocene)
0	Modern		2260*	2260*	0	875	0.00	6.25	100%	
0.3	pre-industrial	2040	2040	2190	−220	655	−1.10	5.15	82%	
8	Holocene	1890	1890	2040	−370	505	−1.85	4.40	70%	
10	Holocene	1880	1880	2030	−380	495	−1.90	4.35	70%	
11.2	Early Holocene	1865	1865	2015	−395	480	−1.98	4.28	68%	100%
13.3	Late glacial	1830	1830	1830	−430	445	−2.15	4.10	66%	96%
16.9	Deglacial	1765	1765	1765	−495	380	−2.48	3.78	60%	88%
18.0	Last Glacial (Glenmore I)	1340	1385°	1385°	−875°	0°	−6.25°			
19.1	Last Glacial (Glenmore III)	1340	1385°	1385°	−875°	0°	−6.25°			

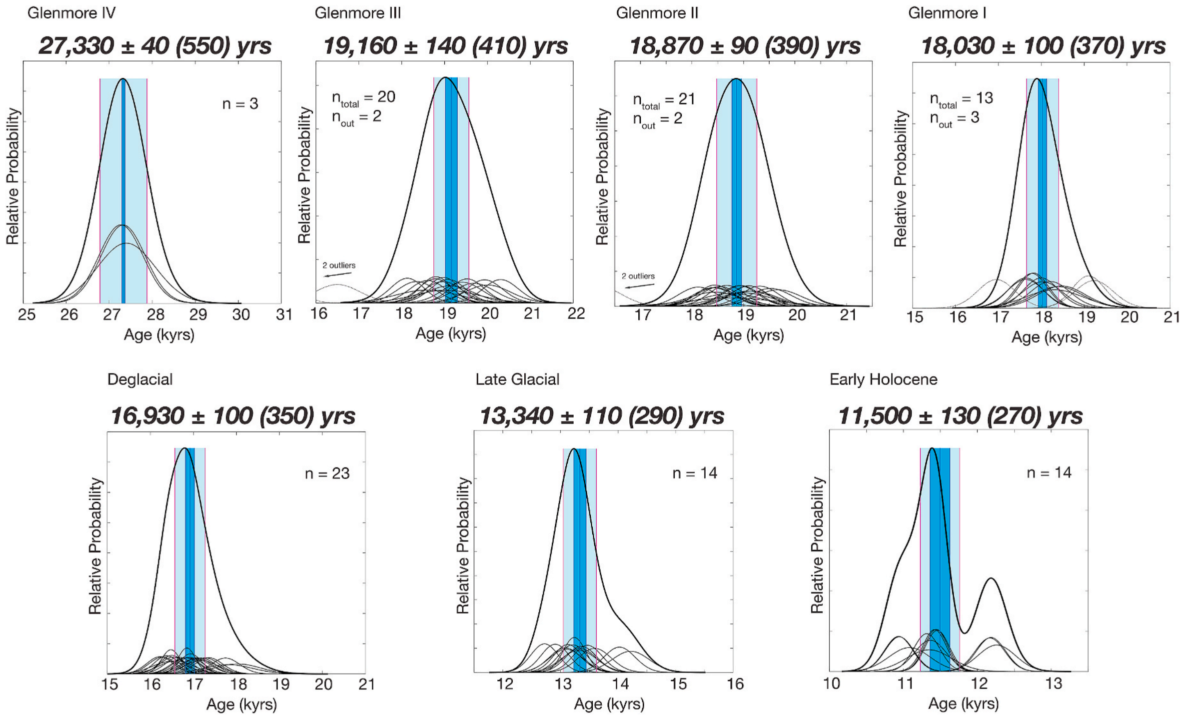

Fig. 4. Normal kernel density functions (i.e., 'camelplots') for dated landform sets in the Takapō/Tekapo catchment. Center blue line is arithmetic mean, while vertical black and purple lines are standard error of the mean (SEM) and production rate uncertainty thresholds, respectively. The thin black curves are the Gaussian representation of each sample. Dotted black lines represent outliers. The thick black curve is the total probability distribution of all plotted samples, excluding outliers. The associated statistics are presented in Table 4.

channel (Cass gorge, Figs. 2 and 6). Upon ice retreat, Lake Takapō/Tekapo initially formed at ~740 m a.s.l., forming a contiguous water body with Lake Alexandrina, before being progressively lowered as its outlet incised (Sutherland et al., 2019a, 2019b). However, the head of the Cass gorge is at ~780 m a.s.l., meaning the lake never reached into the Cass valley. In the Joseph valley (Fig. 6), Sutherland et al. (2019b) identified some poorly expressed, discontinuous post-glacial lake shorelines between ~850 and ~820 m a.s.l., which they attributed to a short-lived ice-contact lake dammed by the Cass glacier tongue. This conclusion is strongly supported by parts of the transverse ridge of glaciogenic sediment being lower than ~800 m a.s.l., thus necessitating ice having been involved in the impoundment. Overall, there is no evidence that a post-glacial lake existed in the Cass valley, providing high confidence that the ELA estimates from deglacial and late-glacial moraines in the upper Cass valley can be interpreted purely in relation to climatic parameters.

Rapid recession of the Takapō/Tekapo glacier system from full-glacial to late-glacial configurations represents an abrupt "jump" between climate modes, with the majority of the glacial to interglacial warming occurring during the first thousand years of the termination. Evidence for large-scale glacier recession between ~18 and ~17 kyrs ago has been documented in the nearby Pukaki, Ohau, and Rakaia valleys (Putnam et al., 2013a, 2013b; Strand et al., 2019; Denton et al., 2021) (Fig. 13), and elsewhere in the Southern Hemisphere

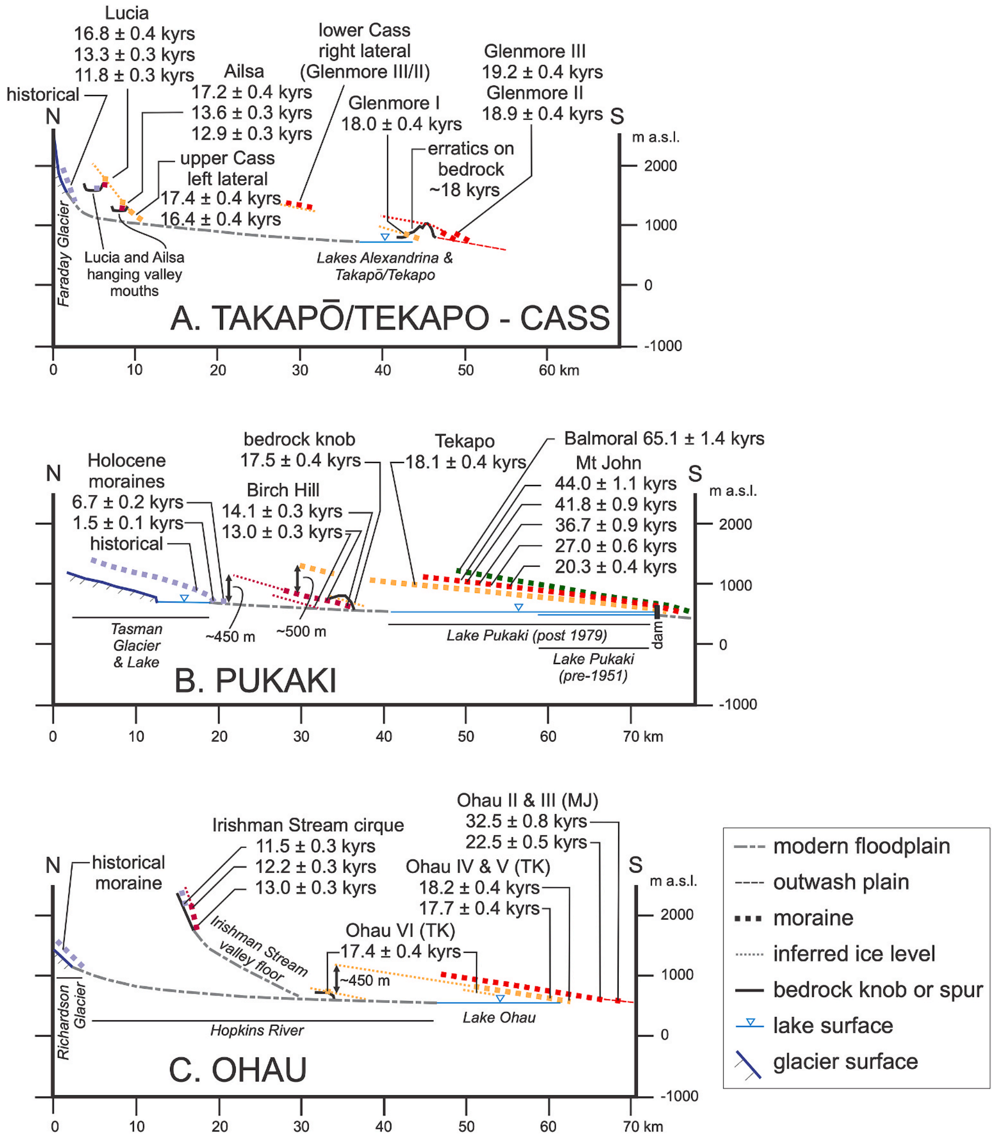

Fig. 5. Geomorphological profile of the Takapō/Tekapo and Cass valleys, location shown in Fig. 2 (A), in comparison to the Pukaki (B) and Ohau (C) valley profiles (both presented and described in Denton et al. (2021)). Valley axis distances in kilometers and elevations above sea level in meters. Mean landform ages for A are discussed in the text.

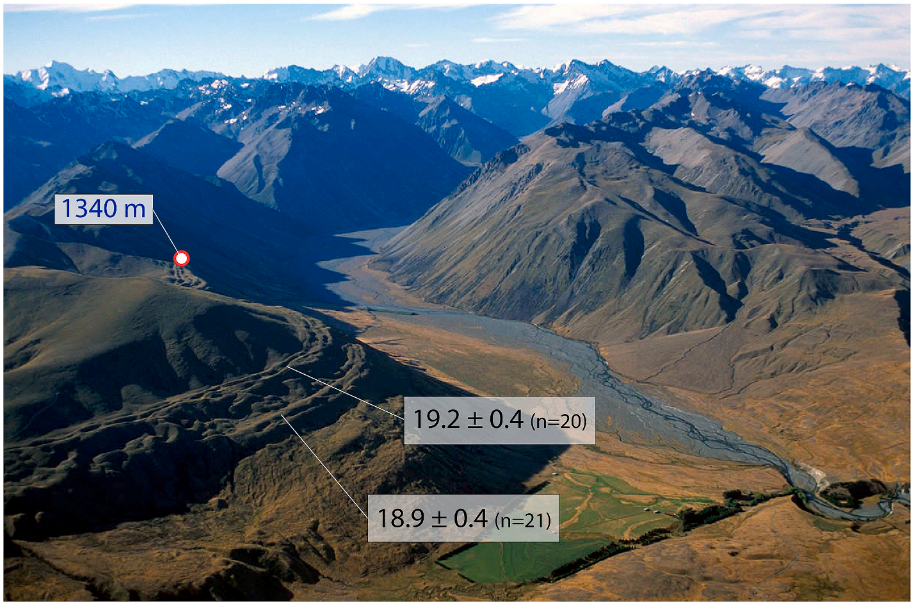

Fig. 6. Aerial view of the Cass valley where it merges with the Takapō/Tekapo main valley, looking west. The two prominent right lateral moraines, based on dating, are parts of the Glenmore III (higher) and Glenmore II (lower) moraine belts, with recessional moraine (lower left; partly equivalent to Glenmore I) inboard of the Glenmore II moraine belt. Ages for the moraine belts are from all samples, not just those collected at this locality, and are listed in kyrs. Up the Cass valley, the lateral moraine ridges end sharply at an elevation of ~1340 m. At lower right is the head of the Cass gorge, through which the river drains to Lake Takapō/Tekapo. At lower center is Joseph valley.

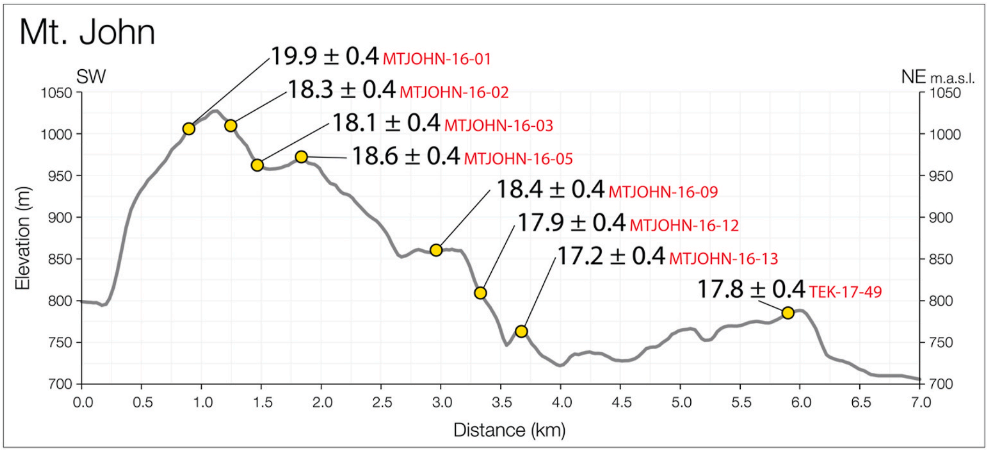

Fig. 7. Topographic profile of the Mt John ice-molded bedrock knob. Ice flow was from right (NE) to left (SW). Yellow dots mark locations of sampled erratic boulders with exposure ages in kyrs. The boulders span ~220 m of altitude and are interpreted to have been deposited by the downwasting glacier ~18,000 years ago.

mid-latitudes, such as Patagonia where rapid deglaciation between ~18 and ~16 kyrs ago (Denton et al., 1999; Strelin et al., 2011; Boex et al., 2013; Hall et al., 2013; Moreno et al., 2015) suggests cohesive climate warming across the South Pacific during Heinrich Stadial 1 (HS 1). Previous evidence for rapid warming is fragmentary due to overrunning of glacial landforms by subsequent glacier activity or general lack of glacier landform preservation, however the moraine chronology from the Takapō/Tekapo catchment allows robustly constrained estimates of climatic amelioration during the last glacial termination.

Atmospheric warming and associated recession of the Takapō/Tekapo glacier at ~18 kyrs ago aligns with a rapid poleward shift of the oceanic subtropical front (STF) (De Deckker et al., 2012, 2020; Moros et al., 2021) and associated southward shift of sea surface temperature (SST) isotherms near New Zealand (Bostock et al., 2015), in addition to pollen-inferred rapid warming on the western flank of the Southern Alps (Vandergoes et al., 2013). At the same time, a top-down breakdown in vertical ocean structure began near the STF during the early phase of the last glacial termination (Allen et al., 2015, 2020). Sustained atmospheric warming was also registered across Antarctica beginning ~18 kyrs ago, including the South Pole (90°S) (Buizert et al., 2021; Kahle et al., 2021). Altogether, these observations indicate that a major change in the Southern Hemisphere climate system took place beginning at ~18 kyrs

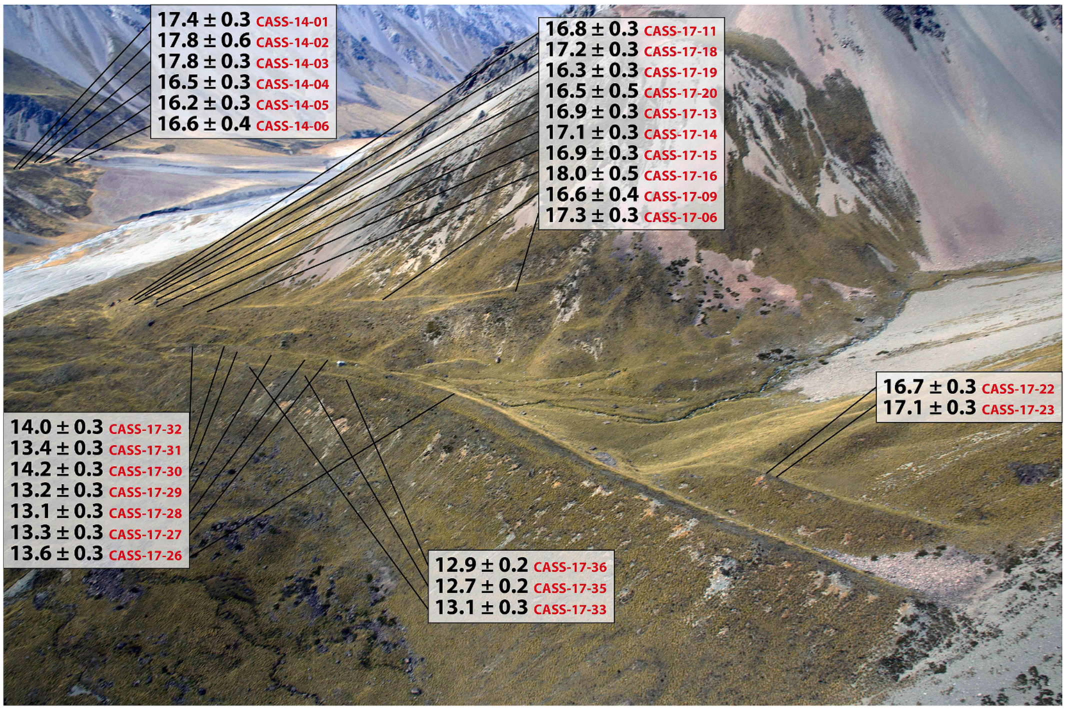

Fig. 8. Aerial view of the moraines of the upper Cass (upper left) and Ailsa (center) valleys, looking downstream to the southeast, with lines pointing to individual sample sites and exposure ages in kyrs.

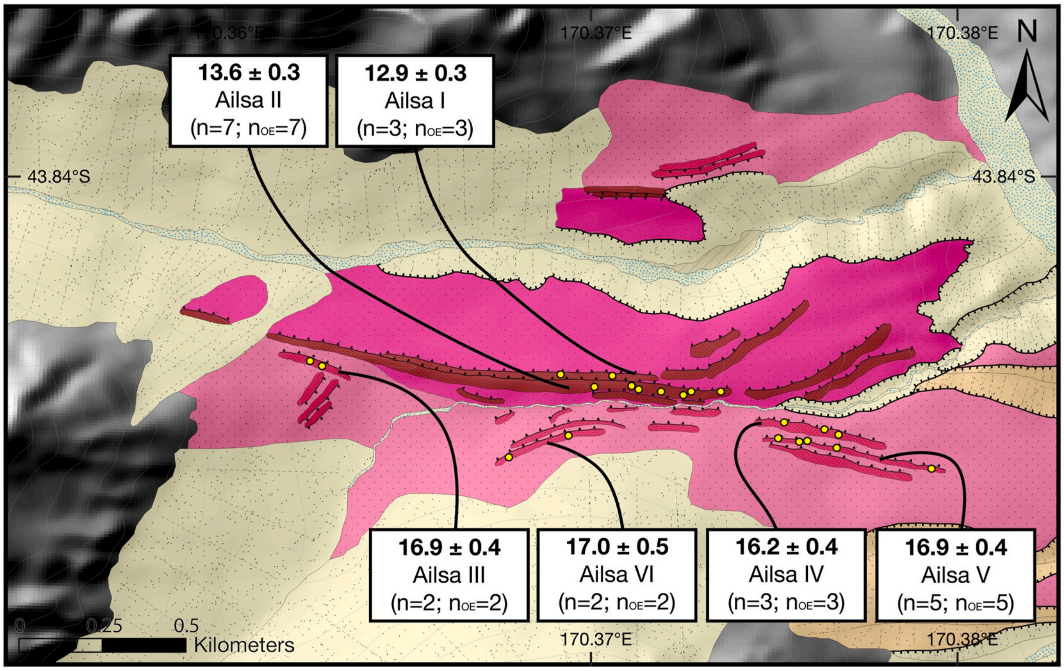

Fig. 9. Glacial geomorphologic map of the Ailsa valley study area (see Fig. 2), with geomorphic symbols equating to those in Fig. 2. Yellow dots are sample locations. Individual ages are shown in Fig. 8, while the mean age for each landform feature is plotted here in kyrs, from age statistics given in Table 4.

ago that impacted atmospheric temperatures, as well as the water mass structure of the Southern Ocean, across the mid-to high southern latitudes. Our glacier-inferred temperature reconstruction reveals that the rate of warming over New Zealand outpaced widely-emphasized climate forcings (Fig. 14). By ~17 kyrs ago, when much of the austral mid-latitude termination was well advanced, atmospheric CO_2 concentration had only risen ~15 ppm, representing ~20% of the full glacial-interglacial CO_2 change (Marcott et al., 2014; Bauska et al., 2021) and atmospheric temperatures registered in interior Antarctica had only risen by ~30% of the full glacial-to-interglacial warming

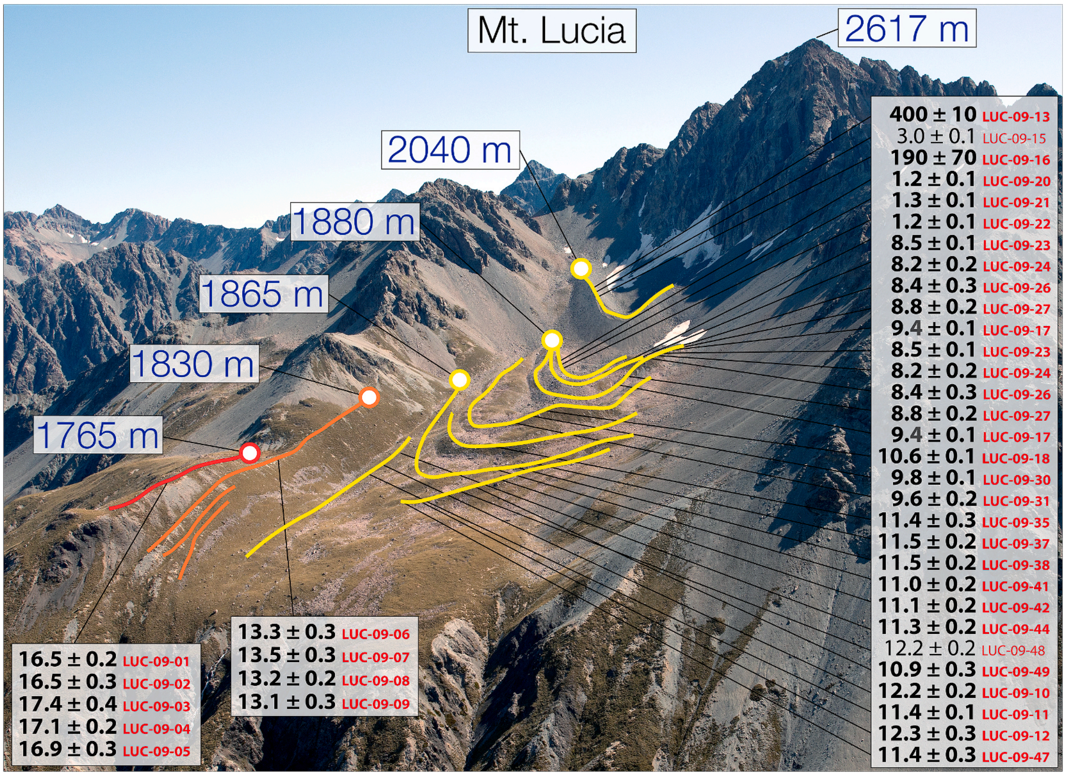

Fig. 10. Aerial view west-southwest to the Lucia valley, with the down-valley lip of the hanging valley at lower center to left. Lines point to individual sample sites, with exposure ages in kyrs (LUC-09-13 and LUC-09-16 in yrs). Ages listed in plain text (not bold) are identified as outliers. Colored lines approximate moraine ridges (red = deglacial, orange = late glacial, yellow = Holocene) and dots mark upper limits of lateral moraines, with elevations (meters above sea level). The ridge geometries highlight the change from a valley-filling glacier during the deglacial and late glacial to a localized source glacier during the Holocene fed mainly from the face of Mt Lucia. The Holocene MELM values shown here have been adjusted to produce ELA values that account for the proportionally higher-elevation ice catchment during the Holocene (Table 5).

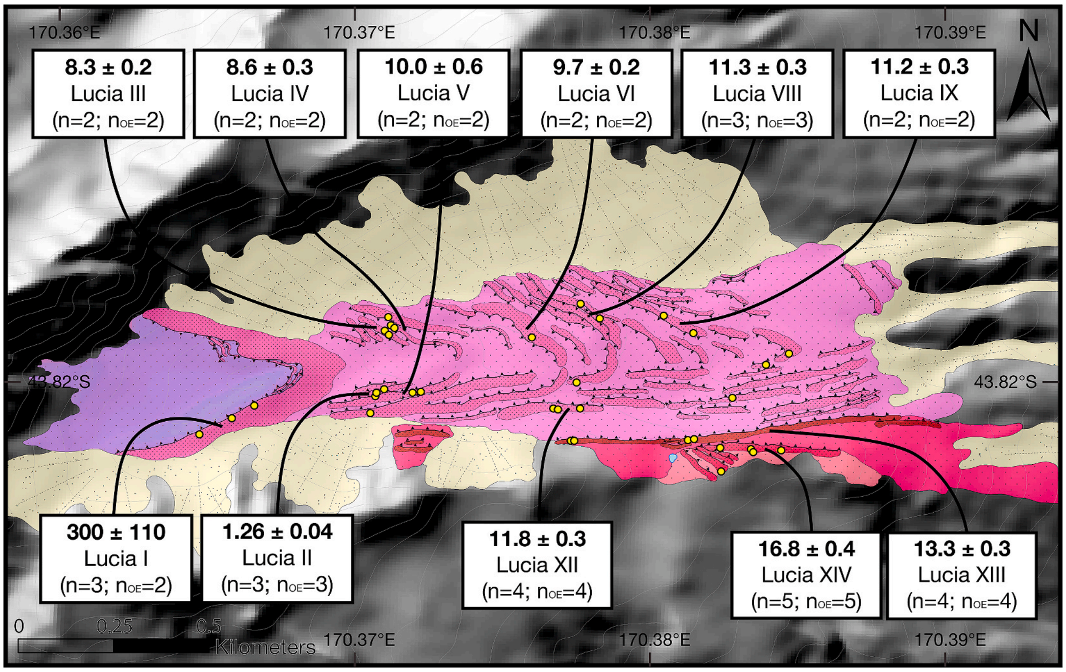

Fig. 11. Glacial geomorphologic map of the Lucia valley study area (see Fig. 2), with geomorphic symbols equating to those in Fig. 2. Yellow dots are sample locations. Individual ages are shown in Fig. 10, while the mean age for each landform feature is plotted here in kyrs, from age statistics given in Table 4.

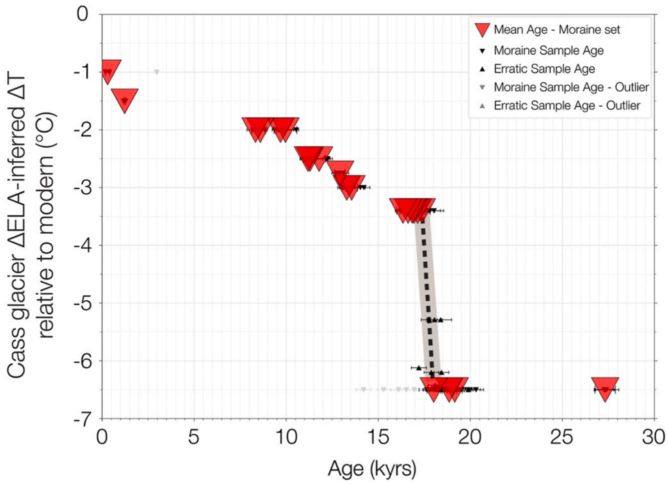

Fig. 12. Cass glacier ΔELA-inferred temperature changes derived from the glacial retreat history. Exposure ages and uncertainties are plotted as triangles and horizontal bars, respectively. Symbols are described in legend, inset. Exposure ages marked as outliers are shown in grey coloring. Dotted black line and grey bars indicate a generalized retreat history based on exposure ages.

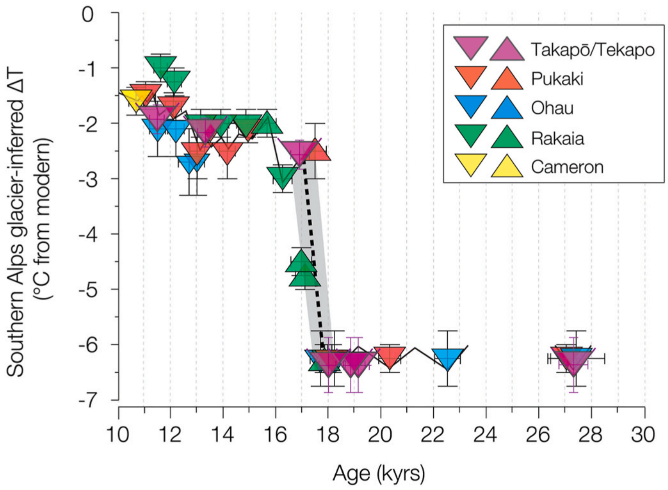

Fig. 13. Glacier-inferred temperatures developed from Southern Alps glacier chronologies (Putnam et al., 2013a, 2013b; Doughty et al., 2015; Kelley et al., 2014; Schaefer et al., 2015; Strand et al., 2019; Denton et al., 2021; this paper). The Cass (Takapō/Tekapo) ΔT values are derived from the MELM-ELA determinations presented here. Ohau ΔT values are derived from numerical glaciological modeling of the Ohau glacier system (Putnam et al., 2013a). Rakaia ΔT values are derived using a different numerical glaciological modeling framework of the Rakaia glacier system (Putnam et al., 2013b). Pukaki ΔT values are from numerical glaciological modeling of Golledge et al. (2012). Cameron ΔT values were determined using ELA techniques, similar to this study (Putnam et al., 2012). This diagram demonstrates compatibility between ELA-inferred temperature changes at different locations in the Southern Alps.

(Buizert et al., 2021; Kahle et al., 2021; Steig et al., 2021) (Fig. 14). The rapid transition between glacial and interglacial modes in the southern mid-latitudes took place several millennia before the combined radiative effects of atmospheric CO_2 and ice-sheet albedo had achieved interglacial levels (Tierney et al., 2020; Osman et al., 2021).

The very rapid rise of atmospheric temperatures over New Zealand compared to atmospheric CO_2 concentration (Marcott et al., 2014; Buizert et al., 2015; Bauska et al., 2021), mean ocean temperature (Bereiter et al., 2018), and warming over Antarctica (Kahle et al., 2021; Steig et al., 2021) at the end of the Last Glaciation suggests that low-frequency forcing components of leading ice age hypotheses are insufficient to explain the abruptness of observed changes (Fig. 14). If true, then the question remains as to what drove the unified and rapid reorganization of the Southern Hemisphere ocean-atmosphere system at the start of the last glacial termination. We posit that the rapid relocation of the austral westerly wind belt to a more southerly position relative to the Zealandia subcontinent at ~18 kyrs ago was the decisive, fast-acting mechanism responsible for translating low-frequency climate forcings, such as orbital changes, into rapid climate warming in the broader region (ie. the Zealandia Swich hypothesis of Denton et al., 2021). This dramatic shift in the austral westerly winds would have bathed Southern Hemisphere mid-latitude glacier systems in relatively warm subtropical air masses, driving the rapid retreat of temperature-sensitive glaciers (Mackintosh et al., 2017; Denton et al., 2021). Important secondary effects of altering wind stresses over the Southern Ocean would have then followed: disruption of Southern Ocean near-surface stratification, increased upwelling of deep water, and degassing of CO_2 into the atmosphere (Anderson et al., 2009; Kohfeld et al., 2013; Sime et al., 2013; Allen et al., 2015, 2020; Gottschalk et al., 2016; Jaccard et al., 2016; Sikes et al., 2023). At the same time, progressive wind-driven ventilation of the deep Southern Ocean would have warmed the surface ocean around Antarctica (as well as the whole global ocean), and in turn warmed the atmosphere over Antarctica – albeit more slowly than over the Southern Hemisphere mid-latitudes. By this mechanism the rapid southward jump of the austral westerlies at ~18,000 yrs ago may have been a unifying factor in driving abrupt deglacial warming in the austral mid-latitudes, and possibly triggering the last glacial termination around the globe by affecting tropical circulation and the western Pacific warm pool, as suggested by the Earth system modeling that supports the Zealandia Switch hypothesis (Denton et al., 2021).

6. Conclusions

- ^{10}Be dating of moraines indicates maxima of ice extent of the Takapō/Tekapo glacier system in the Southern Alps of New Zealand during the global Last Glacial Maximum time period.
- The Cass valley tributary of the Takapō/Tekapo glacier system receded from near-full-glacial to near-interglacial configuration between ~18,000 and ~17,000 yrs ago, resulting from a net atmospheric warming of ~3.8 °C, during which time the glacier retreated ~40 km into the upper reaches of the Cass valley.
- The rapid retreat of the Cass Glacier during the last glacial termination was not an artefact of proglacial lake calving and instead represents a direct response to a shift to notably warmer atmospheric temperature.
- The rapid transition between glacial and interglacial modes throughout the Southern Hemisphere mid-latitudes took place several millennia before the combined radiative effects of atmospheric CO_2 and ice-sheet albedo had achieved interglacial levels.
- Our results are consistent with the Zealandia Switch hypothesis (Denton et al., 2021) which posits non-linear coupled oceanic and atmospheric responses to climate forcing linked to a rapid poleward shift of the austral westerly winds that resulted in abrupt deglacial warming in the Southern Hemisphere mid-latitudes, possibly triggering the last glacial termination around the globe.

Declaration of competing interest

The authors declare that they have no known competing financial

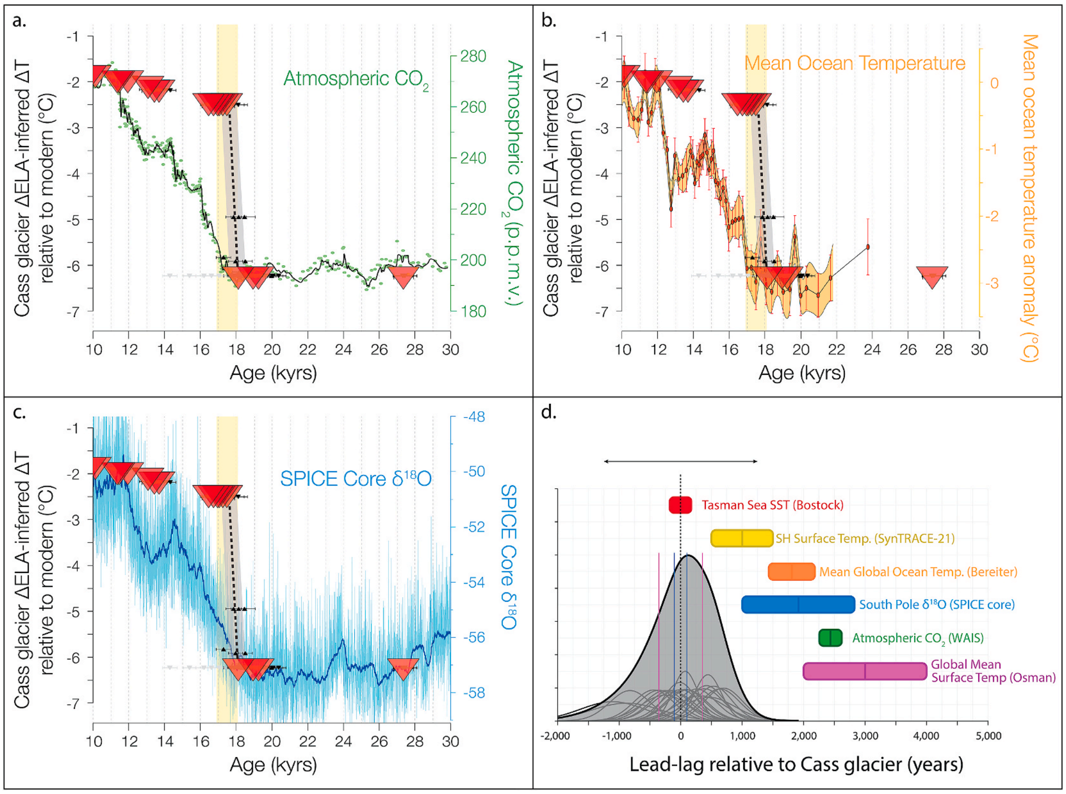

Fig. 14. Cass glacier ΔELA-inferred temperature changes plotted against global climate parameters discussed in text. **a.** Atmospheric CO_2 concentration as measured in Antarctic ice cores (Marcott et al., 2014; Buizert et al., 2015; Bauska et al., 2021). **b.** Mean ocean temperature anomaly (Bereiter et al., 2018) **c.** South Pole SPICE Ice Core $\delta^{18}O$ record from 90°S (Kahle et al., 2021; Steig et al., 2021). **d.** The Cass glacier achieved its late-glacial-equivalent extent during the last glacial termination (~17 kyrs ago). This panel shows the lead (negative x-axis) or lag (positive x-axis) relationship for when selected climate proxies achieved their respective late-glacial-level values during deglaciation, with respect to the mean age of deglacial moraines in the Cass valley.

interests or personal relationships that could have appeared to influence the work reported in this paper.

Data availability

Data will be made available on request.

Acknowledgements

This work was supported by funding from the Comer Family Foundation, the E.R. Quesada Foundation, the Global Climate Change Foundation, and the National Science Foundation. David Barrell was supported by GNS Science. Aaron Putnam acknowledges support from National Science Foundation awards EAR-1554990 and EAR-1903220. We thank Tobias Koffman, Jillian Pelto, Michelle Baumflek, Colin Dowey, Courtney King, Noel Potter, Laura Mattas, Lauren Woods, and Alexzander Roman for their help in the field, and Roseanne Schwartz and Jeremy Frisch for their assistance with laboratory work. We are grateful to Tony and Kura Ritchie and the crew at Lake Ruataniwha Holiday Park for a home-away-from-home during New Zealand field seasons. We thank Glenmore Station, Sawdon Station, Balmoral Station, Mt. Hay Station, Richmond Station, Mt. Gerald Station, New Zealand Department of Conservation - Te Papa Atawhai and Te Runanga o Ngäi Tahu, and the New Zealand Defence Force for generously granting access to study sites. We are grateful to Patrick De Deckker and Peter Almond for providing thoughtful, constructive reviews that greatly helped us improve the clarity and presentation of the manuscript.

Appendix A. Supplementary data

Supplementary data to this article can be found online at https://doi.org/10.1016/j.quascirev.2024.108737.

References

Allen, K.A., Sikes, E.L., Hönisch, B., Elmore, A.C., Guilderson, T.P., Rosenthal, Y., Anderson, R.F., 2015. Southwest Pacific deep water carbonate chemistry linked to high southern latitude climate and atmospheric CO_2 during the Last Glacial Termination. Quat. Sci. Rev. 122, 180–191.

Allen, K.A., Sikes, E.L., Anderson, R.F., Rosenthal, Y., 2020. Rapid loss of CO_2 from the South Pacific Ocean during the last glacial termination. Paleoceanogr. Paleoclimatol. 35, 1–13. https://doi.org/10.1029/2019PA003766.

Anderson, B.M., Mackintosh, A.N., 2006. Temperature change is the major driver of late-glacial and Holocene glacier fluctuations in New Zealand. Geology 34 (2), 121.

Anderson, B.M., Mackintosh, A.N., Stumm, D., George, L., Kerr, T., Winter-Billington, A., Fitzsimons, S.J., 2010. Climate sensitivity of a high-precipitation glacier in New Zealand. J. Glaciol. 56, 114–128.

Anderson, R.F., Ali, S., Bradtmiller, L.I., Nielsen, S.H.H., Fleisher, M.Q., Anderson, B.E., Burckle, L.H., 2009. Wind-driven upwelling in the Southern Ocean and the deglacial rise in atmospheric CO2. Science 323, 1443–1448. https://doi.org/10.1126/science.1167441.

Andrews, J.T., 1975. Glacial Systems: an Approach to Glaciers and Their Environments. Duxbury Press.

Audet, A.C., Putnam, A.E., Russell, J.L., Lorrey, A., Mackintosh, A., Anderson, B., Denton, G.H., 2022. Correspondence among mid-latitude glacier equilibrium line altitudes, atmospheric temperatures, and westerly wind fields. Geophys. Res. Lett. 49 (23) https://doi.org/10.1029/2022GL099897.

Balco, G., Stone, J.O., Lifton, N.A., Dunai, T.J., 2008. A complete and easily accessible means of calculating surface exposure ages or erosion rates from ^{10}Be and ^{26}Al measurements. Quat. Geochronol. 3 (3), 174–195. http://linkinghub.elsevier.com/retrieve/pii/S1871101407000647.

Barker, S., Diz, P., Vautravers, M.J., Pike, J., Knorr, G., Hall, I.R., Broecker, W.S., 2009. Interhemispheric Atlantic seesaw response during the last deglaciation. Nature 457, 1097–1102.

Barrell, D.J.A., 2014. The Balmoral moraines near Lake Pukaki, Southern Alps: a new reference area for the early Otira Glaciation in New Zealand. N. Z. J. Geol. Geophys. 57 (4), 442–452. https://doi.org/10.1080/00288306.2014.936473.

Barrell, D.J.A., Read, S.A.L., 2014. The deglaciation of Lake Pukaki, South Island, New Zealand—a review. N. Z. J. Geol. Geophys. 57, 86–101.

Barrell, D.J.A., Andersen, B.G., Denton, G.H., 2011. Glacial geomorphology of the central South Island, New Zealand. Lower Hutt: GNS Science. GNS Science Monograph 27, 81. + map (5 sheets).

Barrell, D.J.A., Andersen, B.G., Denton, G.H., Smith Lyttle, B., 2013. Glacial geomorphology of the central South Island, New Zealand - digital data. Lower Hutt: GNS Science. GNS Science monograph 27a. Geographic Information System digital data files + explanatory notes 17.

Barrell, D.J.A., Putnam, A.E., Denton, G.H., 2019. Reconciling the onset of deglaciation in the upper Rangitata valley, Southern Alps, New Zealand. Quat. Sci. Rev. 203, 141–150. https://doi.org/10.1016/j.quascirev.2018.11.003.

Bauska, T.K., Marcott, S.A., Brook, E.J., 2021. Abrupt changes in the global carbon cycle during the last glacial period. Nat. Geosci. 14, 91–96. https://doi.org/10.1038/s41561-020-00680-2.

Benn, D.I., Lehmkuhl, F., 2000. Mass balance and equilibrium-line altitudes of glaciers in high-mountain environments. Quat. Int. 65–66, 15–29. https://doi.org/10.1016/S1040-6182(99)00034-8.

Bereiter, B., Shackleton, S., Baggenstos, D., Kawamura, K., Severinghaus, J., 2018. Mean global ocean temperatures during the last glacial transition. Nature 553, 39–44. https://doi.org/10.1038/nature25152.

Boex, J., Fogwill, C., Harrison, S., Glasser, N.F., Hein, A., Schnabel, C., Xu, S., 2013. Rapid thinning of the late Pleistocene Patagonian Ice Sheet followed migration of the Southern Westerlies. Sci. Rep. 3, 1–6. https://doi.org/10.1038/srep02118.

Bostock, H.C., Barrows, T.T., Carter, L., Chase, Z., Cortese, G., Dunbar, G.B., Ellwood, M., Hayward, B., Howard, W.R., Neil, H.L., Noble, T.L., Mackintosh, A.N., Moss, P.T., Moy, A.D., White, D., Williams, M.J.M., Armand, L.K., 2013. A review of the Australian-New Zealand sector of the Southern Ocean over the last 30 ka (Aus-INTIMATE project). Quat. Sci. Rev. 74, 35–57.

Bostock, H.C., Hayward, B.W., Neil, H.L., Sabaa, A.T., Scott, G.H., 2015. Changes in the position of the Subtropical Front south of New Zealand since the last glacial period. Paleooceanography 30, 824-844. https://doi.org/10.1002/2014PA002652.

Broecker, W.S., van Donk, J., 1970. Insolation changes, ice volumes, and the O^{18} record in deep-sea cores. Rev. Geophys. 8, 169–198.

Broecker, W.S., Denton, G.H., 1989. The role of ocean-atmosphere reorganizations in glacial cycles. Geochem. Cosmochim. Acta 53, 2465–2501.

Broecker, W.S., Denton, G.H., 1990. What drives glacial cycles? Sci. Am. 262, 49–56.

Broecker, W.S., 1998. Paleocean circulation during the last deglaciation: a bipolar seesaw? Paleoceanography 13, 119–121.

Broecker, W., 2014. Wally's Carbon World. ELDIGIO Press.

Buizert, C., Cuffey, K.M., Severinghaus, J.P., Baggenstos, D., Fudge, T.J., Steig, E.J., Markle, B.R., Winstrup, M., Rhodes, R.H., Brook, E.J., Sowers, T.A., Clow, G.D., Cheng, H., Edwards, R.L., Sigl, M., McConnell, J.R., Taylor, K.C., 2015. The WAIS Divide deep ice core WD2014 chronology–Part 1: methane synchronization (68–31 ka BP) and the gas age–ice age difference. Clim. Past. 11, 153–173.

Buizert, C., Fudge, T.J., Roberts, W.H.G., Steig, E.J., Sherriff-Tadano, S., Ritz, C., Lefebvre, E., Edwards, J., Kawamura, K., Oyabu, I., Motoyama, H., Kahle, E.C., Jones, T.R., Abe-Ouchi, A., Obase, T., Martin, C., Corr, H., Severinghaus, J.P., Beaudette, R., Epifanio, J.A., Brook, E.J., Martin, K., Chappellaz, J., Aoki, S., Nakazawa, T., Sowers, T.A., Alley, R.B., Ahn, J., Sigl, M., Severi, M., Dunbar, N.W., Svensson, A., Fegyveresi, J.M., He, C., Liu, Z., Zhu, J., Otto-Bliesner, B.L., Lipenkov, V.Y., Kageyama, M., Schwander, J., 2021. Antarctic surface temperature and elevation during the Last Glacial Maximum. Science 372, 1097–1101.

Carter, L., Garlick, R.D., Sutton, P., Chiswell, S., Oien, N.A., Stanton, B.R., 1998. Ocean circulation New Zealand. In: NIWA Chart Miscellaneous Series, 76. NIWA, Wellington, New.

Chinn, T.J.H., Fitzharris, B.B., Willsman, A., Salinger, M.J., 2012. Annual ice volume changes 1976–2008 for the New Zealand Southern Alps. Global Planet. Change 92–93, 105–118.

Chinn, T.J.H., 1995. Glacier fluctuations in the Southern Alps of New Zealand determined from snowline elevations. Arctic Alpine Res. 27, 187–198. https://doi.org/10.2307/1551901.

Chinn, T.J.H., 1999. New Zealand glacier response to climate change of the past 2 decades. Global Planet. Change 22, 155–168.

Chinn, T.J., Heydenrych, C., Salinger, M.J., 2005. Use of the ELA as a practical method of monitoring glacier response to climate in New Zealand's Southern Alps. J. Glaciol. 51, 85–95. https://doi.org/10.3189/172756505781829593.

Clare, G.R., Fitzharris, B.B., Chinn, T.H., Salinger, M.J., 2002. Interannual variation in end-of-summer snowlines of the Southern Alps of New Zealand, and relationships with Southern Hemisphere atmospheric circulation and sea surface temperature patterns. Int. J. Clim. 22, 107–120.

Cox, S.C., Barrell, D.J.A., 2007. Geology of the Aoraki area. Institute of Geological and Nuclear Sciences 1:250,000 geological map. 15.. Wellington, GNS Science. 1 sheet and 71 p.

Crowley, T.J., 1992. North Atlantic deep water cools the Southern Hemisphere. Paleoceanography 7, 489–497. https://doi.org/10.1029/92PA01058.

De Deckker, P., Moros, M., Perner, K., Jansen, E., 2012. Influence of the tropics and southern westerlies on glacial interhemispheric asymmetry. Nat. Geosci. 5 (4), 266–269. https://doi.org/10.1038/ngeo1431.

De Deckker, P., Moros, M., Perner, K., Blanz, T., Wacker, L., Schneider, R., Barrows, T.T., O'Loingsigh, T., Jansen, E., 2020. Climatic evolution in the Australian region over the last 94 ka - spanning human occupancy -, and unveiling the Last Glacial Maximum. Quat. Sci. Rev. 249, 106593 https://doi.org/10.1016/j.quascirev.2020.106593.

Denton, G.H., Lowell, T.V., Heusser, C.J., Schlüchter, C., Andersen, B.G., Heusser, L.E., Moreno, P.I., Marchant, D.R., 1999. Geomorphology, stratigraphy, and radiocarbon chronology of Llanquihue Drift in the area of the southern Lake District, Seno Reloncavi, and Isla Grande de Chiloe, Chile. Geogr. Ann. Phys. Geogr. 81, 167–229.

Denton, G.H., Anderson, R.F., Toggweiler, J.R., Edwards, R.L., Schaefer, J.M., Putnam, A.E., 2010. The last glacial termination. Science 328, 1652–1656. https://doi.org/10.1126/science.1184119.

Denton, G.H., Putnam, A.E., Russell, J.L., Barrell, D.J.A., Schaefer, J.M., Kaplan, M.R., Strand, P.D., 2021. The Zealandia Switch: ice age climate shifts viewed from Southern Hemisphere moraines. Quat. Sci. Rev. 257, 106771 https://doi.org/10.1016/j.quascirev.2020.106771.

Doughty, A.M., Anderson, B.M., Mackintosh, A.N., Kaplan, M.R., Vandergoes, M.J., Barrell, D.J.A., Denton, G.H., Schaefer, J.M., Chinn, T.J.H., Putnam, A.E., 2013. Evaluation of lateglacial temperatures in the Southern Alps of New Zealand based on glacier modelling at Irishman Stream, Ben Ohau Range. Quat. Sci. Rev. 74, 160–169. https://doi.org/10.1016/j.quascirev.2012.09.013.

Doughty, A.M., Schaefer, J.M., Putnam, A.E., Denton, G.H., 2015. Mismatch of glacier extent and summer insolation in Southern Hemisphere mid-latitudes. Geology. 43, 407–410. https://doi.org/10.1130/G36477.1.

Eaves, S.R., Anderson, B.M., Mackintosh, A.N., 2017. Glacier-based climate reconstructions for the last glacial-interglacial transition: Arthur's Pass, New Zealand (43°S). J. Quat. Sci. 32 (6), 877–887.

Gottschalk, J., Skinner, L.C., Lippold, J., Vogel, H., Frank, N., Jaccard, S.L., Waelbroeck, C., 2016. Biological and physical controls in the Southern Ocean on past millennial-scale atmospheric CO$_2$ changes. Nat. Commun. 7, 11539. https://doi.org/10.1038/ncomms11539.

Golledge, N.R., Mackintosh, A.N., Anderson, B.M., Buckley, K.M., Doughty, A.M., Barrell, D.J.A., Denton, G.H., Vandergoes, M.J., Andersen, B.G., Schaefer, J.M., 2012. Last Glacial Maximum climate in New Zealand inferred from a modelled Southern Alps icefield. Quat. Sci. Rev. 46, 30–45. https://doi.org/10.1016/j.quascirev.2012.05.004.

Hall, B.L., Porter, C.T., Denton, G.H., Lowell, T.V., Bromley, G.R.M., 2013. Extensive recession of Cordillera Darwin glaciers in southernmost South America during Heinrich Stadial 1. Quat. Sci. Rev. 62, 49–55.

Harrington, H.J., 1952. Glacier wasting and retreat in the Southern Alps of New Zealand. J. Glaciol. 2, 140–145.

Hogg, A.G., Heaton, T.J., Hua, Q., Palmer, J.G., Turney, C.S.M., Southon, J., Bayliss, A., Blackwell, P.G., Boswijk, G., Bronk Ramsey, C., Pearson, C., Petchey, F., Reimer, P., Reimer, R., Wacker, L., 2020. SHCal20 Southern Hemisphere calibration, 0-55,000 years cal BP. Radiocarbon 62 (4), 759–778. https://doi.org/10.1017/RDC.2020.59.

Jaccard, S.L., Galbraith, E.D., Martínez-Garciá, A., Anderson, R.F., 2016. Covariation of deep Southern Ocean oxygenation and atmospheric CO$_2$ through the last ice age. Nature 530 (7589), 207–210. https://doi.org/10.1038/nature16514.

Kahle, E.C., Steig, E.J., Jones, T.R., Fudge, T.J., Koutnik, M.R., Morris, V.A., Vaughn, B. H., Schauer, A.J., Stevens, C.M., Conway, H., Waddington, E.D., Buizert, C., Epifanio, J., White, J.W.C., 2021. Reconstruction of temperature, accumulation rate, and layer thinning from an ice core at South Pole, using a statistical inverse method. J. Geophys. Res. Atmos. https://doi.org/10.1029/2020jd033300.

Kaplan, M.R., Schaefer, J.M., Denton, G.H., Barrell, D.J.A., Chinn, T.J.H., Putnam, A.E., Andersen, B.G., Finkel, R.C., Schwartz, R., Doughty, A.M., 2010. Glacier retreat in New Zealand during the Younger Dryas stadial. Nature 467, 194–197. https://doi.org/10.1038/nature09313.

Kaplan, M.R., Schaefer, J.M., Denton, G.H., Doughty, A.M., Barrell, D.J.A., Chinn, T.J.H., Putnam, A.E., Andersen, B.G., Mackintosh, A., Finkel, R.C., Schwartz, R., Anderson, B., 2013. The anatomy of long-term warming since 15 ka in New Zealand based on net glacier snowline rise. Geology 41, 887–890. https://doi.org/10.1130/G34288.1.

Kelley, S.E., Kaplan, M.R., Schaefer, J.M., Andersen, B.G., Barrell, D.J.A., Putnam, A.E., Denton, G.H., Schwartz, R., Finkel, R.C., Doughty, A.M., 2014. High-precision ^{10}Be chronology of moraines in the Southern Alps indicates synchronous cooling in Antarctica and New Zealand 42,000 years ago. Earth Planet Sci. Lett. 405, 194–206.

Kelly, M.A., Lowell, T.V., Hall, B.L., Schaefer, J.M., Finkel, R.C., Goehring, B.M., Alley, R. B., Denton, G.H., 2008. A ^{10}Be chronology of lateglacial and Holocene mountain glaciation in the Scoresby Sund region, east Greenland: implications for seasonality during lateglacial time. Quat. Sci. Rev. 27, 2273–2282.

Kohfeld, K.E., Graham, R.M., de Boer, A.M., Sime, L.C., Wolff, E.W., Le Quéré, C., Bopp, L., 2013. Southern Hemisphere westerly wind changes during the Last Glacial Maximum: paleo-data synthesis. Quat. Sci. Rev. 68 (C), 76–95. https://doi.org/10.1016/j.quascirev.2013.01.017.

Koffman, T.N.B., Schaefer, J.M., Putnam, A.E., Denton, G.H., Barrell, D.J.A., Rowan, A. V., Finkel, R.C., Rood, D.H., Schwartz, R., Plummer, M.A., Brocklehurst, S.H., 2017. A beryllium-10 chronology of late-glacial moraines in the upper Rakaia valley, Southern Alps, New Zealand supports Southern-Hemisphere warming during the Younger Dryas. Quat. Sci. Rev. 170, 14–25. https://doi.org/10.1016/J.QUASCIREV.2017.06.012.

Lal, D., 1991. Cosmic ray labeling of erosion surfaces: *in situ* nuclide production rates and erosion models. Earth Planet Sci. Lett. 104, 424–439.

Lichtenecker, N., 1938. Die gegenwartige und die eiszeit liche Schneegrenze in den Ostalpen. Verhandlungsband Der III, vol. 1936. Internationalen Quartarkonferenz, Wien, pp. 141–147.

Lifton, N., Smart, D.F., Shea, M.A., 2008. Scaling time-integrated in situ cosmogenic nuclide production rates using a continuous geomagnetic model. Earth Planet Sci. Lett. 268 (1–2), 190–201. https://doi.org/10.1016/j.epsl.2008.01.021.

Lifton, N., Sato, T., Dunai, T.J., 2014. Scaling *in situ* cosmogenic nuclide production rates using analytical approximations to atmospheric cosmic-ray fluxes. Earth Planet Sci. Lett. 386, 149–160. http://dx.doi.org/10.1016/j.epsl.2013.10.052.

Lifton, N.A., Phillips, F.M., Cerling, T.E., 2016. Chapter 9 - using Lake Bonneville features to calibrate in situ cosmogenic nuclide production rates. In: Oviatt, C.G., Shroder, J. F.B.T.-D., E, S.P. (Eds.), Lake Bonneville. Elsevier, pp. 165–183. https://doi.org/10.1016/B978-0-444-63590-7.00009-3.

Lorrey, A.M., Vargo, L., Purdie, H., Anderson, B., Cullen, N.J., Sirguey, P., Mackintosh, A., Willsman, A., Macara, G., Chinn, W., 2022. Southern Alps equilibrium line altitudes: four decades of observations show coherent glacier-climate responses and a rising snowline trend. J. Glaciol. 1127–1140 https://doi.org/10.1017/jog.2022.27.

Mackintosh, A.N., Anderson, B.M., Pierrehumbert, R.T., 2017. Reconstructing climate from glaciers. Annu. Rev. Earth Planet Sci. 45 (1), 649–680. http://www.annualreviews.org/doi/10.1146/annurev-earth-063016-020643.

Marcott, S.A., Bauska, T.K., Buizert, C., Steig, E.J., Rosen, J.L., Cuffey, K.M., Fudge, T.J., Severinghaus, J.P., Ahn, J., Kalk, M.L., McConnell, J.R., Sowers, T., Taylor, K.C., White, J.W.C., Brook, E.J., 2014. Centennial-scale changes in the global carbon cycle during the last deglaciation. Nature 514, 616–619. https://doi.org/10.1038/nature13799.

Marcott, S.A., Clark, P.U., Shakun, J.D., Brook, E.J., Davis, P.T., Caffee, M.W., 2019. ^{10}Be age constraints on latest Pleistocene and Holocene cirque glaciation across the western United States. NPJ Clim Atmos Sci 2. https://doi.org/10.1038/s41612-019-0062.

Meierding, T.C., 1982. Late Pleistocene glacial equilibrium-line altitudes in the Colorado Front Range: a comparison of methods. Quat. Res. 18 (3), 289–310. https://doi.org/10.1016/0033-5894(82)90076.

Moreno, P.I., Denton, G.H., Moreno, H., Lowell, T.V., Putnam, A.E., Kaplan, M.R., 2015. Radiocarbon chronology of the last glacial maximum and its termination in northwestern Patagonia. Quat. Sci. Rev. 122, 233–249.

Moros, M., De Deckker, P., Perner, K., Ninnemann, U.S., Wacker, L., Telford, R., Jansen, E., Blanz, T., Schneider, R., 2021. Hydrographic shifts south of Australia over the last deglaciation and possible interhemispheric linkages. Quat. Res. 102, 130–141. https://doi.org/10.1017/qua.2021.12.

Nishiizumi, K., Imamura, M., Caffee, M.W., Southon, J.R., Finkel, R.C., McAninch, J., 2007. Absolute calibration of ^{10}Be AMS standards. Nucl. Instrum. Methods Phys. Res. B 258, 403–413.

Norton, D.A., 1985. A multivariate technique for estimating New Zealand temperature normals. Weather Clim. 5, 64–74.

Oerlemans, J., 1994. Quantifying global warming from the retreat of glaciers. Science 264, 243–245.

Oerlemans, J., 1997. Climate sensitivity of Franz Josef Glacier, New Zealand, as revealed by numerical modeling. Arct. Alp. Res. 29 (2), 233–239. https://doi.org/10.2307/1552052.

Osman, M.B., Tierney, J.E., Zhu, J., Tardif, R., Hakim, G.J., King, J., Poulsen, C.J., 2021. Globally Resolved Surface Temperatures since the Last Glacial Maximum. Nature 599, 239–244. https://doi.org/10.1038/s41586-021-03984-4.

Porter, S.C., 1975. Equilibrium-line altitudes of late Quaternary glaciers in the Southern Alps, New Zealand. Quat. Res. 5 (1), 27–47. https://doi.org/10.1016/0033-5894(75)90047-2.

Putnam, A.E., Schaefer, J.M., Barrell, D.J.A., Vandergoes, M.J., Denton, G.H., Kaplan, M.R., Finkel, R.C., Schwartz, R., Goehring, B.M., Kelley, S.E., 2010. In situ cosmogenic ^{10}Be production-rate calibration from the Southern Alps, New Zealand. Quat. Geochronol. 5, 392–409. https://doi.org/10.1016/j.quageo.2009.12.001.

Putnam, A.E., Schaefer, J.M., Denton, G.H., Barrell, D.J.A., Finkel, R.C., Andersen, B.G., Schwartz, R., Chinn, T.J.H., Doughty, A.M., 2012. Regional climate control of glaciers in New Zealand and Europe during the pre-industrial Holocene. Nat. Geosci. 5, 627–630. https://doi.org/10.1038/ngeo1548.

Putnam, A.E., Schaefer, J.M., Denton, G.H., Barrell, D.J.A., Birkel, S.D., Andersen, B.G., Kaplan, M.R., Finkel, R.C., Schwartz, R., Doughty, A.M., 2013a. The last glacial maximum at 44S documented by a 10Be moraine chronology at Lake Ohau, southern Alps of New Zealand. Quat. Sci. Rev. 62, 114–141.

Putnam, A.E., Schaefer, J.M., Denton, G.H., Barrell, D.J.A., Andersen, B.G., Koffman, T.N.B., Rowan, A. v, Finkel, R.C., Rood, D.H., Schwartz, R., Vandergoes, M.J., Plummer, M.A., Brocklehurst, S.H., Kelley, S.E., Ladig, K.L., 2013b. Warming and glacier recession in the Rakaia valley, southern Alps of New Zealand, during Heinrich stadial 1. Earth Planet Sci. Lett. 382, 98–110.

Putnam, A.E., Bromley, G.R.M., Rademaker, K., Schaefer, J.M., 2019. *In situ* ^{10}Be production-rate calibration from a ^{14}C-dated late-glacial moraine belt in Rannoch Moor, central Scottish Highlands. Quat. Geochronol. 50, 109–125. https://doi.org/10.1016/j.quageo.2018.11.006.

Rother, H., Fink, D., Shulmeister, J., Mifsud, C., Evans, M., Pugh, J., 2014. The early rise and late demise of New Zealand's last glacial maximum. Proc. Natl. Acad. Sci. USA 111, 11630–11635. https://doi.org/10.1073/pnas.1401547111.

Rother, H., Shulmeister, J., Fink, D., Alexander, D., Bell, D., 2015. Surface exposure chronology of the Waimakariri glacial sequence in the Southern Alps of New Zealand: implications for MIS-2 ice extent and LGM glacial mass balance. Earth Planet Sci. Lett. 429, 69–81. https://doi.org/10.1016/j.epsl.2015.07.033.

Schaefer, J.M., Denton, G.H., Barrell, D.J.A., Ivy Ochs, S., Kubik, P.W., Andersen, B.G., Phillips, F.M., Lowell, T.V., Schlüchter, C., 2006. Near-synchronous interhemispheric termination of the last glacial maximum in mid-latitudes. Science 312 (5779), 1510–1513.

Schaefer, J.M., Denton, G.H., Kaplan, M.R., Putnam, A.E., Finkel, R.C., Barrell, D.J.A., Andersen, B.G., Schwartz, R., Mackintosh, A.N., Chinn, T.J.H., Schluchter, C., 2009. High-frequency Holocene glacier fluctuations in New Zealand differ from the northern signature. Science 324, 622–625.

Schaefer, J.M., Putnam, A.E., Denton, G.H., Kaplan, M.R., Birkel, S., Doughty, A.M., Kelley, S., Barrell, D.J.A., Finkel, R.C., Winckler, G., Anderson, R.F., Ninneman, U.S., Barker, S., Schwartz, R., Andersen, B.G., Schluechter, C., 2015. The southern glacial maximum 65,000 years ago and its unfinished termination. Quat. Sci. Rev. 114, 52–60.

Shakun, J.D., Clark, P.U., He, F., Marcott, S.A., Mix, A.C., Liu, Z., Otto-Bliesner, B.L., Schmittner, A., Bard, E., 2012. Global warming preceded by increasing carbon dioxide concentrations during the last deglaciation. Nature 484 (7392), 49–54. https://doi.org/10.1038/nature10915.

Sikes, E.L., Umling, N.E., Allen, K.A., Ninnemann, U.S., Robinson, R.S., Russell, J.L., Williams, T.J., 2023. Southern Ocean glacial conditions and their influence on deglacial events. Nat. Rev. Earth Environ. 4, 454–470. https://doi.org/10.1038/s43017-023-00436-7.

Sime, L.C., Kohfeld, K.E., Le Quéré, C., Wolff, E.W., de Boer, A.M., Graham, R.M., Bopp, L., 2013. Southern Hemisphere westerly wind changes during the Last Glacial Maximum: model-data comparison. Quat. Sci. Rev. 64 (C), 104–120. https://doi.org/10.1016/j.quascirev.2012.12.008.

Steig, E.J., Jones, T.R., Schauer, A.J., Kahle, E.C., Morris, V.A., Vaughn, B.H., Davidge, L., White, J.W.C., 2021. Continuous-flow analysis of δ^{17}O, δ^{18}O, and δD of H_2O on an ice core from the South Pole. Front. Earth Sci. 9, 1–14. https://doi.org/10.3389/feart.2021.640292.

Stone, J.O., 2000. Air pressure and cosmogenic isotope production. J. Geophys. Res. Solid Earth, 105 (B10), 23,753-23,759.

Strand, P.D., Schaefer, J.M., Putnam, A.E., Denton, G.H., Barrell, D.J.A., Koffman, T.N.B., Schwartz, R., 2019. Millennial-scale pulsebeat of glaciation in the Southern Alps of New Zealand. Quat. Sci. Rev. 220, 165–177. https://doi.org/10.1016/j.quascirev.2019.07.022.

Strelin, J.A., Denton, G.H., Vandergoes, M.J., Ninnemann, U.S., Putnam, A.E., 2011. Radiocarbon chronology of the late-glacial Puerto Bandera moraines, Southern Patagonian Icefield, Argentina. Quat. Sci. Rev. 30, 2551–2569.

Stuiver, M., Polach, H.A., 1977. Discussion: Reporting of ^{14}C data. Radiocarbon 19, 355–363. https://doi.org/10.1017/S0033822200003672.

Suggate, R.P., Almond, P.C., 2005. The Last Glacial Maximum (LGM) in western South Island, New Zealand: implications for the global LGM and MIS 2. Quat. Sci. Rev. 24 (16), 1923–1940. http://www.sciencedirect.com/science/article/pii/S0277379104003324.

Sutherland, J.L., Carrivick, J.L., Shulmeister, J., Quincey, D.J., James, W.H.M., 2019a. Ice-contact proglacial lakes associated with the Last Glacial Maximum across the Southern Alps, New Zealand. Quat. Sci. Rev. 213, 67–92. https://doi.org/10.1016/j.quascirev.2019.03.035.

Sutherland, J.L., Carrivick, J.L., Evans, D.J.A., Shulmeister, J., Quincey, D.J., 2019b. The Tekapo Glacier, New Zealand, during the Last Glacial Maximum: An active temperate glacier influenced by intermittent surge activity. Geomorphology 343, 183–210. https://doi.org/10.1016/j.geomorph.2019.07.008.

Sutherland, J.L., Carrivick, J.L., Gandy, N., Shulmeister, J., Quincey, D.J., Cornford, S.L., 2020. Proglacial lakes control glacier geometry and behavior during recession. Geophys. Res. Lett. 47, article e2020GL088865. doi:10.1029/2020GL088865.

Sutherland, J.L., Evans, D.J.A., Carrivick, J.L., Rother, H., Sutherland, J.L., Evans, D.J.A., Carrivick, J.L., 2022. A model of ice-marginal sediment-landform development at Lake Tekapo, Southern Alps, New Zealand. Geogr. Ann. Phys. Geogr. 104 (3), 151–182. https://doi.org/10.1080/04353676.2022.2084591.

Tielidze, L.G., Eaves, S.R., Norton, K.P., Mackintosh, A.N., Hidy, A.J., 2022. Cosmogenic ^{10}Be constraints on deglacial snowline rise in the Southern Alps, New Zealand. Quat. Sci. Rev. 286, 107548 https://doi.org/10.1016/j.quascirev.2022.107548.

Tielidze, L.G., Eaves, S.R., Norton, K.P., Mackintosh, A.N., Pedro, J.B., Hidy, A.J., 2023. Early glacier advance in New Zealand during the Antarctic Cold Reversal. J. Quat. Sci. 38 (4), 544–562. https://doi.org/10.1002/jqs.3495.

Tierney, J.E., Zhu, J., King, J., Malevich, S.B., Hakim, G.J., Poulsen, C.J., 2020. Glacial cooling and climate sensitivity revisited. Nature 584, 569–573. https://doi.org/10.1038/s41586-020-2617-x.

Vandergoes, M.J., Dieffenbacher-Krall, A.C., Newnham, R.M., Denton, G.H., Blaauw, M., 2008. Cooling and changing seasonality in the Southern Alps, New Zealand during the Antarctic Cold Reversal. Quat. Sci. Rev. 27, 589–601.

Vandergoes, M.J., Newnham, R.M., Denton, G.H., Blaauw, M., Barrell, D.J.A., 2013. The anatomy of Last Glacial Maximum climate variations in south Westland, New Zealand, derived from pollen records. Quat. Sci. Rev. 74, 215–229. https://doi.org/10.1016/j.quascirev.2013.04.015.